SYNTHESIS AND CHARACTERIZATION OF TIN IV OXIDE (SnO_2) NANOPARTICLES FOR ENERGY APPLICATIONS

BY

RANIA AFIA NUAMAH
(ID NO.: 10336720)

UNIVERSITY OF GHANA, LEGON
COLLEGE OF BASIC AND APPLIED SCIENCES
DEPARTMENT OF MATERIALS SCIENCE AND ENGINEERING

THIS THESIS IS SUBMITTED TO THE
UNIVERSITY OF GHANA, LEGON IN PARTIAL FULFILMENT OF THE REQUIREMENT FOR THE AWARD OF MPHIL MATERIALS SCIENCE AND ENGINEERING DEGREE.

2016

SYNTHESIS AND CHARACTERIZATION OF TIN IV OXIDE (SnO_2) NANOPARTICLES FOR ENERGY APPLICATIONS

BY

RANIA AFIA NUAMAH
(ID NO: 10336720)

UNIVERSITY OF GHANA, LEGON
COLLEGE OF BASIC AND APPLIED SCIENCES
DEPARTMENT OF MATERIALS SCIENCE AND ENGINEERING,

THIS THESIS IS SUBMITTED TO THE UNIVERSITY OF GHANA, LEGON IN PARTIAL FULFILMENT OF THE REQUIREMENT FOR THE AWARD OF MPHIL MATERIALS SCIENCE AND ENGINEERING DEGREE.

JULY 2016

Email: afianuamah@yahoo.com

DECLARATIONS

Candidate's Declaration

I hereby declare that this MPhil thesis which is the result of my own original research under strict supervision was prepared in accordance with the University of Ghana's academic regulations and that no part of it has been presented for another degree in this University or elsewhere.

Candidate's name: ..... **Miss Rania Afia Nuamah**.....

Signature: .....Date: .....**11th July, 2016**.....

Supervisors' declaration

We hereby declare that the preparation and presentation of this MPhil thesis were supervised in accordance with the guidelines on supervision of MPhil thesis laid down by the University of Ghana.

Supervisor: …….**Dr. David Dodoo-Arhin**……..

Signature..... Date: …... **11th July, 2016**……..

Co-supervisor: **Prof. Pushpendra Kumar Jain**……

Signature….R K Jain……Date: …….**11th July, 2016**……

Head of Department's declaration

I hereby declare that this MPhil thesis has been prepared, supervised and accepted in accordance with the guidelines on the MPhil thesis laid down by the University of Ghana.

Head of Department's name: ……**Dr. David Dodoo-Arhin**…….....

Signature.....Date: **18th July, 2016**……

ABSTRACT

Electrochemical capacitors (ECs) or Supercapacitors (SCs) are energy saving devices which have excellent properties that include high power density, long cycle life, low temperature sensitivity and low maintenance cost. However these devices have lower energy densities than conventional batteries. To improve on its energy density, SnO_2 which is a metal oxide was considered as an electrode material because of its chemical inertness and thermal stability.

SnO_2 nanoparticles were synthesized using the hydrothermal and water-in-oil microemulsion techniques. Well crystalline particles with different morphologies and crystallite size in the range of 2nm to 10nm were obtained by using Urea and Soduim Borohydride as reducing agents, Dioctyl Sulfosuccinate sodium salt (**AOT)** and Cetyl Trimethyl ammonium bromide **(CTAB)** as the surfactants in the hydrothermal techniques. X-ray diffractometry, Scanning Electron microscopy, Energy Dispersive X-ray spectroscopy and Fourier Transform Infrared spectroscopy revealed the presence of tin oxide (SnO_2). The electrochemical properties were investigated using cyclic voltammetry, electrochemical impedance spectroscopy and potentiostatic charge-discharge in aqueous KOH electrolyte. The SnO_2 electrode material showed properties as a pseudocapacitor with a maximum capacitance value of 1.6 Fg^{-1} at a scan rate of 5 mVs^{-1}, an efficiency of 52 % at a current of 1mA and a maximum capacitance retention of about 40% after 10 cycles at a current of 1 mA.

From the results obtained it can be concluded that Sodium borohydride is a better reducing agent in the synthesis of SnO_2 nanoparticles. Also, although the crystallite size of the SnO_2 particles were small they exhibited very low pseudocapacitance as a result of the low conductivity of the nanoparticles and the lack of electrochemical active sites. To improve on

the capacitance of the SnO_2 nanoparticles, conductive carbon can be added and composite SnO_2 composite materials with carbonaceous materials can also be an alternative.

ACKNOWLEDGEMENTS

My sincere gratitude goes to the almighty God for giving me life and strength to be able to complete this MPhil research thesis work. My profound gratitude goes to the African Materials Science and Engineering Network (AMSEN), Science Initiative Group of the Regional Initiative on Science Education (SIG-RISE) with support from the Carnegie Corporation of New York for funding my MPhil program.

I also thank my supervisors Dr. David Dodoo-Arhin (supervisor- University of Ghana) and Prof. P.K Jain (co-supervisor- University of Botswana) for their immense contribution towards my MPhil research thesis work. I thank all the lecturers and students of the Department of Materials Science and Engineering and the entire School as a whole for making my years of studies at the University of Ghana a successful one.

DEDICATION

I dedicate this thesis to my parents, Mr Yaw Opuni and Madam Alice Asare and my siblings for their advice, support and care throughout my life. I also dedicate this thesis to everyone who has played an important role in my life.

TABLE OF CONTENTS

LIST OF TABLES

LIST OF FIGURES

LIST OF ACRONYMS

AOT	Dioctyl Sulfosuccinate sodium salt
BET	Brunner Emmet Teller
CCCD	Constant Current Charge/Discharge
CNT's	Carbon nanotubes
CTAB	Cetyl Trimethyl ammonium bromide
CV	Cyclic voltammetry
ECs	Electrochemical Capacitors
EDLC	Electrical Double Layer Capacitance
ESR	Equivalent Series Resistance
SnO_2	Tin (iv) oxide
TCOs	Transparent Conducting Oxides
TEMABF4	Triethylmethylammonium tetrafluoroborate
W/O	Water-in-oil
XRD	X-Ray Diffraction
Z_{dia}	Real axis

CHAPTER ONE

1.0 Introduction

For some time now, considerable efforts have been made to develop new energy storage devices which have high energy and high power density to meet the worlds demand for clean energy. Supercapacitors (SCs) which are also known as Electrochemical Capacitors (ECs) are a kind of promising energy storage devices. They can produce a large amount of energy in a short period of time and they are usually preferred for energy storage systems due to their excellent cyclability and very good power performance as compared to conventional capacitors and batteries [1]. Supercapacitors currently, are used in a wide range of consumer electronics, memory back-up systems, and industrial power and energy management. A new development as far as supercapacitors are concerned is their use in emergency doors on Airbus A380. Another promising application is their use in low-emission hybrid electric vehicles and fuel cell vehicles to serve as a temporary energy storage device with a high-power capability to store energies when braking. Supercapacitors can be grouped into two types, (Electrical Double Layer Capacitor and Pseudocapacitor), according to their charge/discharge mechanisms [2]. The Electrical Double Layer Capacitor stores energy by electrostatic adsorption/desorption between polarized solid electrode vertical line liquid electrolyte interfaces, and Pseudocapacitor stores energy by surface faradaic redox reactions on the interface of the electroactive material and the electrolyte. The large capacitance of the Pseudocapacitor is possible by electrode material that can be reversibly oxidized and reduced over a wide potential range [2-4].

The major electrode materials that are used in supercapacitors are those made of graphene and other carbonaceous materials (carbon nanotubes, activated carbon, etc.). The desire to use carbon materials come from the fact that they store the charges electrostatically using

reversible adsorption of ions of the electrolyte onto active materials that are electrochemically stable and have a high accessible surface area. However, their low specific charge has made scientists look into finding new materials which are environmentally friendly and have high energy storage capacity [5]. Transition metal oxides have also been studied widely for use as electrode materials for supercapacitors. Although RuO_2 has good capacitive properties as a supercapacitor electrode material (specific capacitance: 1300 Fg^{-1}) [6], its toxic nature, rarity and high production cost will exclude it from wide and commercial applications. Manganese oxide is another transition metal oxide studied as an electrode material for supercapacitor application. Manganese can exist in three different valence states and its oxides are highly complex. The capacitance of manganese oxides theoretically, reaches to 1100 Cg^{-1} (from Mn (IV) to Mn (III)) but the electrochemical reversibility of redox transition of manganese dioxide is usually too low to be applicable, and the pure manganese dioxide possess poor capacitive response due to high resistance of bulk manganese oxide [7].

Tin dioxide (SnO_2), a transparent conducting oxide and a wide band gap n-type semiconductor, has been used in many applications such as gas sensors, electrodes in solid-state ionic devices, solar cells, etc., due to its unique properties such as chemically inert, mechanically hard, and thermally heat stability. Only one stable phase (there is no metastable one) is known, which has a tetragonal arrangement of the atoms exhibiting either a rutile or cassiterite structure. Tin dioxide can be synthesized using a variety of techniques such as sol-gel, hydrothermal method, precipitation, carbothermal reduction and polymeric precursor. Techniques such as precipitation provide particle sizes of less surface area and smaller pore size as a result of agglomeration, which makes them unsuitable for applications such as gas sensors, electrode materials for supercapacitors and batteries as compared to hydrothermal and microemulsions techniques [8-10].

The objectives of this research are to synthesize tin dioxide nanoparticles via the hydrothermal technique under mild conditions (120°C) and water-in-oil microemulsions technique, characterize the as-synthesized particles and use the as-synthesize particles in a supercapacitor application. In order to be able to realize the objectives mentioned afore, different base additives, urea and sodium borohydride, will be used to determine their effects on the tin oxide nanoparticles. Physical and electrochemical characterizations such as X-ray Diffraction, Brunner Emmet Teller (BET) technique, transmission electron microscopy, and cyclic voltammetry measurements shall be used to determine the phase, surface area and pore size, particle size, charge and discharge properties of the as-synthesized tin oxide particles.

This thesis has been organized into five chapters: First chapter gives an overview of the background of study, the key objectives, and how the results of this work could be used. Chapter two examines the relevant theories from both an appreciative inquiry and critical analysis point and gives some perspectives on some empirical works in the area. Chapter three gives the experimental design of the study and the key analytical methods. The fourth chapter presents the results and discussions of the findings and Chapter five draws conclusions and makes recommendations.

CHAPTER TWO

2.0 Literature Review

In this section nanomaterials and supercapacitors will be discussed. The various materials used for supercapacitors along with their pros and cons will also be elaborated. Current methods of preparation of tin dioxide nanoparticles will be discussed with much focus on the hydrothermal and microemulsions route of synthesizing tin dioxide nanoparticles.

2.1 Nanoscience and Nanotechnology

Nanotechnology was first introduced in the famous lecture of Nobel laureate Richard P. Feynman, "There's Plenty of Room at the Bottom", given in 1959 at California Institute of Technology [11]. Since then, there have been developments in physics, chemistry and biology over the years which have proven Feynman's ideas of manipulating and controlling matter at extremely small scale, even to the level of molecules and atoms, i.e. nanoscale. Nanotechnology refers to any technology performed on a nanoscale that has applications in the real world. It deals with the production and application of physical, chemical and biological systems at scales ranging from a few nanometers to submicron dimensions, as well as integration of the resulting nanostructures into larger systems. Changes occur significantly in materials when their particle or grain size is decreased from the macrosize to nanosize and properties such as chemical reactivity, mechanical properties and others are also affected [11].

2.1.1 Properties of Nanomaterials

Nanostructure materials are single phase or multiphase polycrystalline solids with a typical average particle size of a few nanometers (1nm = 10^{-9}m). Nanomaterials are usually in the range of 1 to 100 nm, [12] according to the National Nanotechnology Initiative in the US. The

size of hydrogen atom is considered as the lower limit of nano whereas upper limit is arbitrary. The grain sizes are so small; a significant volume fraction of the atoms resides in grain boundaries. Material is characterized by a large number of interfaces in which the atomic arrangements are different from those of crystal lattice. The basic classification of nonmaterial is done based on the confinement. Bulk structures show no confinement whereas nano-wells and nanowires can be obtained by 2-D and 1-D confinement respectively. The quantum realm comes to the picture when there is a 3-D confinement and leads to zero-dimension quantum structures that is quantum dot. Recent trends in Electrochemical Supercapacitors (ES) also involve the development of nanostructured materials, such as nanoaerogels, nanotubes/rods, nanoplates, nanospheres, and so on. Nanostructured materials possess high specific surface area. They can provide short transport/diffusion path lengths for ions and electrons, leading to faster kinetics, more efficient contact of electrolyte ions, and more electroactive sites for faradaic energy storage, resulting in high charge/discharge capacities even at high current densities. Material morphology is closely related to the specific surface area and the diffusion of ions in the electrode, and one-dimensional nanostructure materials seem to be very promising for ES application due to their reduced diffusion paths and larger specific surface areas [13].

2.2 Structure and main bulk properties of Tin Dioxide

Tin dioxide is a semiconductor material, transparent, of high chemical and mechanical stability. Only one stable phase is known, which has a tetragonal arrangement of the atoms receiving the names of either rutile or cassiterite. The heat of formation is, $H = 1.9 * 10^3$ J mol^{-1}, the heat capacity of the material is, $Cp = 52.59$ J mol^{-1} K^{-1}, the density at 300 K is 6.95 g cm^{-3} and the melting point is 1630^0C. This crystalline structure contains metal atoms in octahedral coordination and oxygen in planar three-coordination. Lattice parameters are a =

4.737 Å (a=b in the tetragonal structure) and c = 3.186 Å. The atomic position at 300 K in the unit cell is (0, 0, 0) and (½, ½, ½) for the metal and ± (u, u, 0) and (½+u, ½-u, ½), being u=0.387, for the oxygen. The rest of the atoms of the unit cell can be obtained applying the rutile symmetry D^{14}_{4h} (C_{2v}, $P4_2/mnm$ point group). Chemical bonding is mainly governed by the linear combination of oxygen 2s and 2p orbitals with tin 5s and 5p orbitals. With respect to its chemical properties, tin dioxide has a high chemical stability, as it is only attacked by hot concentrated alkalis, this being one of the reasons of the wide research done with this material [12]. It is well known that the size and the morphology of the nanomaterials greatly affect their properties as well as their applications due to their high surface-to volume ratio, enhanced characteristics of quantum size effects, and high fraction of chemically similar surface sites [14].

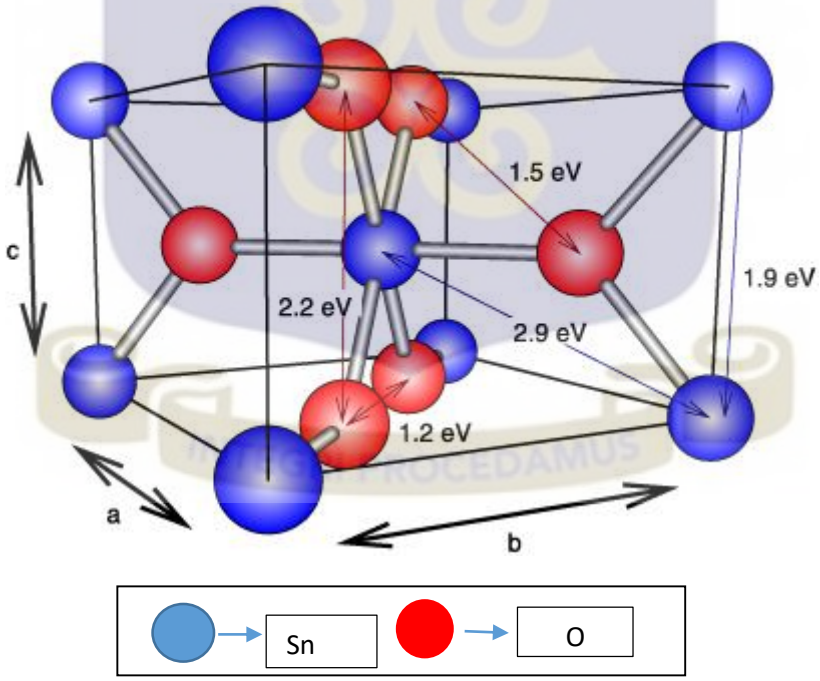

Figure 2.1: Crystal structure of tin dioxide (SnO_2) [15]

2.2.1 Comparison between stannic (SnO_2) and stannous oxide (SnO)

Oxides of tin exist in two main forms: stannic oxide (SnO_2) and stannous oxide (SnO). These two oxides show the dual valency nature of tin, with oxidation states of 2+ and 4+. SnO_2 is better characterized than stannous oxide (SnO). For instance, SnO's electronic band gap is not accurately known but lies somewhere in the range of 2.5–3 eV. Thus SnO exhibits a smaller band gap than SnO_2, which is commonly quoted to be 3.6 eV [15]. A detailed studies of stannous oxide cannot be facilitated due to the non-availability of single crystals of stannous oxide. Stannic oxide has the rutile structure and stannous oxide has the less common litharge structure. Stannic oxide the more abundant form of tin oxide and is of technological importance in gas sensing applications and oxidation catalysts. There also exists a slightly denser orthorhombic high pressure phase in addition to the common rutile (tetragonal) structured SnO_2 phase. Figure 2.2 shows the Sn–O phase diagram for atmospheric pressure. The diagram indicates the existence of an intermediate tin-oxide phase between SnO and SnO_2 at elevated temperature. In these intermediate oxides Sn is present as a mixture of Sn (II) and Sn (IV). Stannic oxide is the thermodynamically most stable form of tin oxide[16].

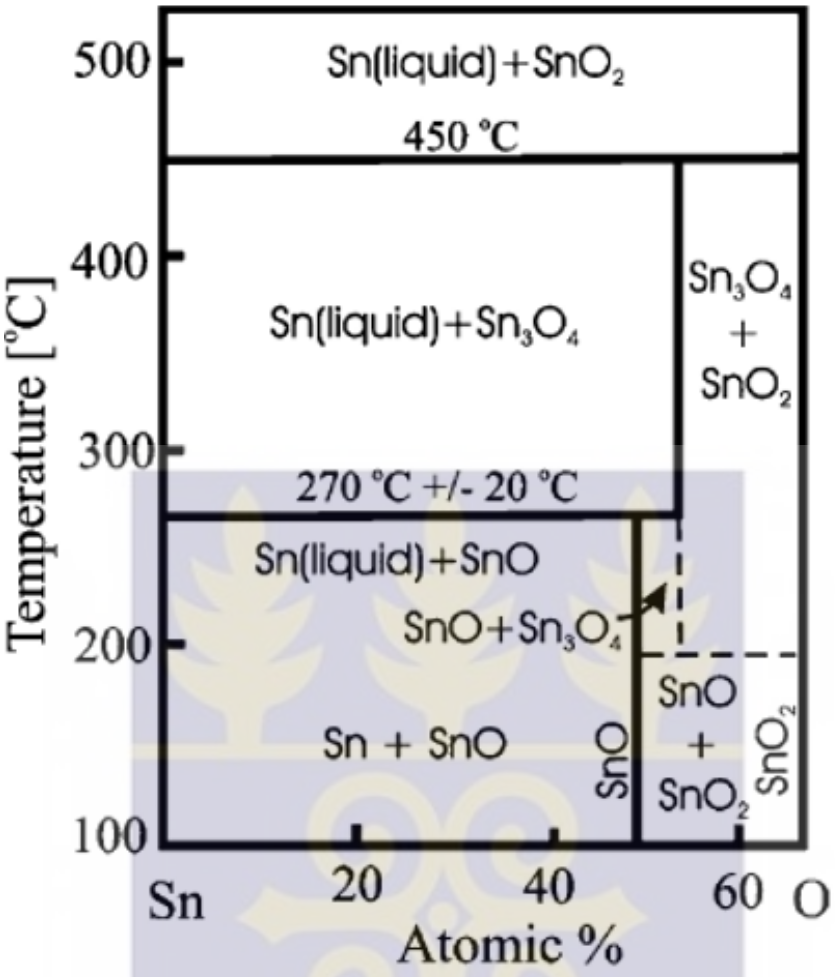

Figure 2.2: Sn-O phase diagram [15]

2.3 Applications of tin dioxide (SnO_2)

Tin dioxide is in the class of materials that have high electrical conductivity with optical transparency and as such constitutes an important component for optoelectronic applications [16].

2.3.1 Transparent conductors

SnO_2 belongs to the oxide materials family that combine low electrical resistance with high optical transparency in the visible range of the electromagnetic spectrum. These properties are useful in a number of applications; notably as electrode materials in solar cells, light emitting

diodes, flat panel displays, and other optoelectronic devices where an electric contact needs to be made without obstructing photons from either entering or escaping the optical active area, and in transparent electronics such as transparent field effect transistors. Another property of SnO_2 and other Transparent Conducting Oxides (TCOs) is that although they are transparent in the visible spectral range they are highly reflective for infrared radiation. This property is reason for the dominant use of SnO_2 as an energy conserving material. Architectural windows coated with SnO_2, for example, allow transmitting light but keeping the heat out or in the building depending on the climate region. More sophisticated architectural windows, rely on TCOs to electrically contact electrochromic films that change their coloring and transparency by applying a voltage across the films. There is a large number of TCOs, the most commonly known ones are the binary systems, i.e. SnO_2, ZnO, and In_2O_3. Often the highest possible conductivity is sought. Many of the binary TCOs already possess a high conductivity due to intrinsic defects, i.e. oxygen deficiencies. This is also the case for SnO_2, which, as a wide band-gap semiconductor, is in its stoichiometric form a good insulator. Non-stoichiometry, in particular oxygen deficiency, makes it a conductor [16].

2.3.2 Heterogeneous catalysis

Many oxides act as a support material for dispersed metal catalysts; however, tin dioxide, is an oxidation catalyst in its own right. Tin-oxide based catalysts show good activity towards CO/O_2 and CO/NO reactions. In most oxide catalysts the oxidation reactions are supposed to follow the Mars–van Krevelen mechanism. In the Mars-van Krevelen mechanism, the molecules are oxidized by consuming lattice oxygen of the oxide catalyst which in turn is re-oxidized by gas-phase oxygen. This is possible because transition and post transition oxides have multivalent oxidation states that allow the material to easily give up lattice oxygen to react with adsorbed molecules and can be subsequently re-oxidize by gas-phase oxygen. It is shown that surfaces with Sn^{4+} or Sn^{2+} are stable for different oxygen chemical potentials.

Which is an indication that, an easy re-oxidation and reduction of SnO_2 surfaces can be expected in catalytic oxidation reactions [16].

2.3.3 Solid state gas sensors

Gas sensing materials can be made from materials that change their properties depending on the ambient conditions. Normally, changes in the electrical conductance in response to environmental gases are monitored. For instance, all the following oxides show a gas response in their conductivity: Mn_2O_3, NiO, Co_3O_4, CuO, CdO, MgO, SrO, BaO, In_2O_3, WO_3, La_2O_3, TiO_2, V_2O_3, Fe_2O_3, GeO_2, Cr_2O_3, Nb_2O_5, MoO_3, Ta_2O_5, CeO_2, Nd_2O_3. ZnO and SnO_2 however, are the most commonly used gas sensing materials. Bulk- and surface-sensitive materials are the main divisions of gas sensitivity of oxides. For example, TiO_2 increases its conductivity due to the formation of bulk oxygen vacancies under reducing conditions and is thus categorized as a bulk sensitive gas sensing material. On the other hand, SnO_2, although bulk defects affect its conductivity, belongs to the category of surface sensitive materials [15].

2.4 Electrochemical Capacitors (Supercapacitors)

It's a device that stores electrical energy in the electrical double layer that forms at the interface between an electrolytic solution and an electronic conductor [17]. According to the Rangone plot in Figure 2.3, supercapacitors have very good properties in terms of the specific energy as well the specific power in comparison to batteries [18, 19]. High-capacitance supercapacitors and the overall capacitance of the electrode materials can be realized when the pseudo capacitance due to the presence of foreign electro-active species is coupled with the Electrical Double Layer Capacitance (EDLC) [18]. The ultimate performance of the supercapacitor can be achieved when the most critical aspects which is to optimize the energy

density without reducing their power capability is paid attention to. The use of high-capacitance materials (high surface area or pseudo-active species) ensures high energy density. For EDLC's, carbonaceous materials such as carbon aerogel is an ideal electrode material as it allows an interconnected three- dimensional network structure, a high specific surface-area, good electrical conductivity and a suitable pore size for common electrolytes [2]. Transition metal oxides such as RuO_2, NiO, MnO_2 and SnO_2 and conducting polymers with various oxidation states are considered as promising materials for Pseudocapacitors as they generate their capacitance from the reversible redox transitions of the electroactive materials [2].

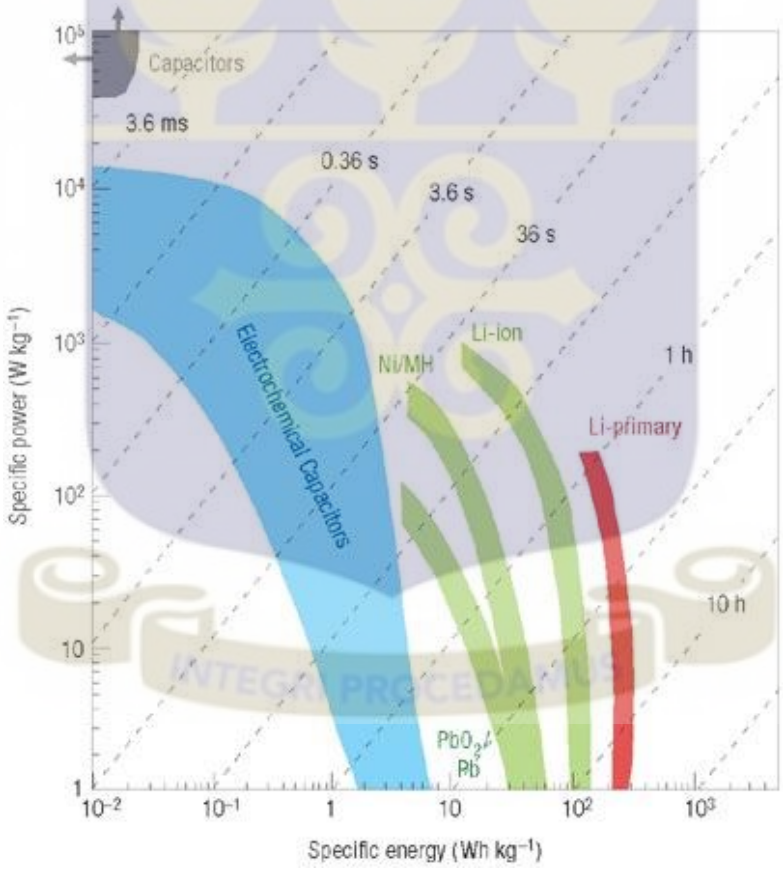

Figure 2.3: Ragone plot showing the specific power against specific energy for different Electrochemical Devices [18].

2.4.1 Electric Double Layer Capacitors (EDLC's)

Electric double layer capacitor (EDLC) is an electrical storage device, which stores much more energy than conventional capacitors and offer much higher power density than batteries. EDLC works on the principle of double-layer capacitance at the electrode/electrolyte interface where electric charges are accumulated on the electrode surfaces and ions of opposite charge are arranged on the electrolyte side. The electrode material used for the construction of the cell EDLC is mainly carbon material (activated carbon, carbon nanotubes and graphene) [1]. Although activated carbon has a high specific surface area, the low electrical conductivity of activated carbon limits its applications in high power density supercapacitors for example, a commercial activated carbon for supercapacitors can only achieve a specific capacitance of 26 Fg^{-1}). Carbon nanotubes (CNT's) which have been studied to replace activated carbon for supercapacitors because of their excellent electrical conductivity and high surface area unfortunately showed a low energy density as reported by Cheng et.al. [1].

The electrolytes can be either aqueous or non-aqueous depending on the mode of construction of EDLC cell. Since 1978 EDLCs based on carbon electrodes have been used for memory back-up device for many electrical appliances like camera and VCRs. The EDLCs in 1980s were used for the energy source to drive wrist watches with solar cells. In 1990s, they were used as actuator back-up sources for toys, electric appliances, home equipment and others. Recently, EDLCs with higher capacitances are under development for higher electric power sources in electric vehicle systems and electric power storage systems. Specific capacitance theoretically, of an activated carbon is directly proportional to the specific surface area. In reality however, it does not happen. A major disadvantage of carbon based EDLC is the lower specific stored energy. To rectify these problems, researchers now incorporate transition metal oxides along with carbon in the electrode materials. When the electrode materials consist of transition metal oxides, then the electrosorption or redox processes enhance the

value of specific capacitance for 10-100 times depending on the nature of oxides. In such a situation the EDLC is called a hybrid supercapacitor [7].

Thus, the development of electroactive materials with high specific surface areas, such as nanostructured metal oxides becomes a trend in order to increase the performance of supercapacitors. These electrode materials generally show the combined characteristics of high double-layer capacitance and Faradaic pseudocapacitance, resulting in the significant increase in both energy density and power density [19]. As reported by Wang and Hu [18] the addition of SnO_2 into RuO_2 matrix considerably increased the electrochemical stability and the electrochemically active sites of RuO_2 coatings. During the process of charging, the electrons travel from the negative electrode to the positive electrode through an external load. Within the electrolyte, cations move towards the negative electrode while anions move towards the positive electrode. During discharge, the reverse processes take place. In this type of ES, no charge transfers across the electrode/ electrolyte interface, and no net ion exchanges occur between the electrode and the electrolyte. This implies that the electrolyte concentration remains constant during the charging and discharging processes. In this way, energy is stored in the double-layer interface [20].

Carbon composites with transition metal oxides such as SnO_2, RuO_2 and MnO_2 as electrode materials for SCs have shown very good specific capacitance. Qian Chen et al [1] reported on SCs using MnO_2-coated graphene electrode which exhibited a high specific capacitance of 328 Fg^{-1} as compared to the graphene electrode supercapacitor which had a specific capacitance of 245 F g^{-1}. EDLCs have low energy density and

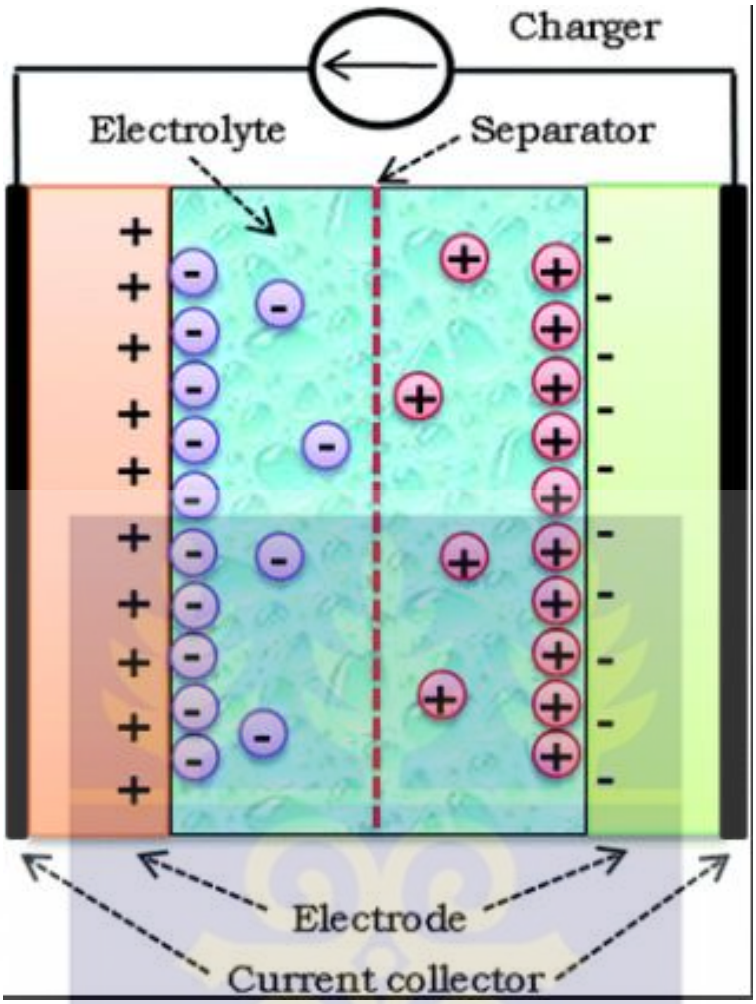

Figure 2.4: Schematic Diagram of an EDLC [21]

2.4.2 Pseudocapacitors/ Faradaic Supercapacitors (FS)

The term "Pseudocapacitance" is usually used to describe the behavior of electrode materials (MnO_2, RuO_2) that have the electrochemical signature of a capacitive electrode, that is, a linear dependence of the charge stored with changing potential within the window of interest, but in which charge storage originates from electron-transfer mechanisms, rather than simply relying on the accumulation of ions in the electrochemical double layer (as with activated carbons). When a potential is applied to a FS, fast and reversible faradaic reactions (redox reactions) take place on the electrode materials and involve the passage of charge across the double layer, similar to the charging and discharging processes that occur in batteries, resulting in faradaic current passing through the supercapacitor cell [20]. Materials

undergoing such redox reactions include conducting polymers and several metal oxides, including RuO_2, MnO_2, and Co_3O. Reversible adsorption (for example, adsorption of hydrogen on the surface of platinum or gold), redox reactions of transition metal oxides (e.g. RuO_2), and reversible electrochemical doping–dedoping in conductive polymer based electrodes are the three types of faradaic processes occur at FS electrodes. It has been proven that these faradaic electrochemical processes not only increase the working voltage but also increase the specific capacitance of the supercapacitors. An FS exhibits far larger capacitance values and energy density than an EDLS since the electrochemical processes occur both on the surface and in the bulk near the surface of the solid electrode, [20].

2.4.3 Factors affecting the Capacitance of Supercapacitors

- Particle sizes,
- Concentration of electrolyte,
- Scan rate,
- Surface activation under the electrochemical conditions,
- Surface oxygen content,
- Surface oxides, and
- Lattice defects resulting from the method of preparation [20].

2.4.4 Electrolyte

The general requirements for an electrolyte in ES include: high electrochemical stability, wide voltage window, high ionic concentration, low solvated ionic radius, low resistivity, low viscosity, low volatility, low toxicity, low cost as well as availability of constituent chemicals of high purity. The electrolyte used in an ES can be classified into three types: (1) aqueous electrolyte, (2) organic electrolyte, and (3) ionic liquids (ILs).

(1) ***Aqueous electrolyte:*** aqueous electrolytes (such as H_2SO_4, Na_2SO_4, KOH and NH_4Cl aqueous solution), compared with organic electrolytes can give a higher ionic concentration and lower resistance. ES containing aqueous electrolyte may display higher capacitance and higher power than those with organic electrolytes, probably due to higher ionic concentration and smaller ionic radius. Also, aqueous electrolytes can be utilized and prepared without strictly controlling the preparing processes and conditions, while organic ones need strict processes and conditions to obtain ultra-pure electrolytes.

A large disadvantage of aqueous electrolytes unfortunately, is their small voltage window (1.2 V) which much lower than those of organic electrolytes. Aqueous electrolytes have a big limitation in terms of improving both power densities and energy as a result of their narrow voltage window. This is one of the main reasons why organic electrolytes are often recommended [20].

(2) ***Organic electrolyte:*** Organic electrolytes can provide a voltage window as high as 3.5 V compared to aqueous electrolytes. This is one big advantage of organic over aqueous electrolytes. Acetonitrile and propylene carbonate (PC) are the most commonly used solvents among organic electrolytes. Larger amounts of salt can be dissolved with Acetonitrile than other solvents, but suffers from environmental and toxic problems. PC-based electrolytes are environmentally friendly and can offer a wide electrochemical window, a wide range of operating temperature, as well as good conductivity. Besides, organic salts such as tetraethylammonium tetrafluoroborate, tetraethylphosphonium tetrafluoroborate, and triethylmethylammonium tetrafluoroborate (TEMABF4) have also been used in ES electrolytes. Salts with less symmetric structures have lower crystal-lattice energy and increased solubility. However, one issue which should be kept in mind is that the water content in organic electrolytes must be kept below 3–5 ppm. Otherwise, the ES's voltage will be significantly reduced [20].

(3) **Ionic liquids (ILs):** A salt may be turned into a 'liquid', by providing heat to the system to counterbalance the salt lattice energy. Such a system is called molten salts or ILs. ILs can exist in liquid form at the desired temperatures. Their desirable properties make them promising candidates for ES electrolytes. These properties include low vapor pressure, high thermal and chemical stability, low flammability, wide electrochemical stability window ranging from 2 to 6 V, typically about 4.5 V, and conductivity at a level of ca. 10 $mScm^{-1}$ [21]. Since ILs are solvent-free, there is no solvation shell in ILs, and thus ILs can offer a well identified ion size. The main ILs studied for ES applications are imidazolium, pyrrolidinium, as well as asymmetric, aliphatic quaternary ammonium salts with anions such as tetrafluoroborate, trifluoromethanesulfonate, bis(trifluoromethanesulfonyl) imide, bis(fluorosulfonyl)imide or hexafluorophosphate. Room temperature ILs are usually quaternary ammonium salts such as tetralkylammonium $[R_4N]^+$, and cyclic amines such as aromatic pyridinium, imidazolium and saturated piperidinium, pyrrolidinium. Low temperature molten salts based on sulfonium $[R_3S]^+$ as well as phosphonium $[R_4P]^+$ cations are also explored in the literature [22]. The chemical–physical properties of these ILs strongly depend on the type of cation and anion. For example, aliphatic quaternary ammonium and pyrrolidinium salts display a wider potential range, sometimes exceeding 5 V, but their conductivity is generally lower than that of 1-ethyl-3- methylimidazolium-based ILs which remain liquid down to low temperature (< -50°C) and display higher conductivities as high as 10^{-2} S cm^{-1} at room temperature. A number of electrodes and devices have been prepared using ILs. For example, ethyl-methyl imidazolium-bis(trifluoromethane- sulfonyl)imide was used to investigate the relationship between the pore size of carbon electrodes, ion size of the electrolyte, and the capacitance.1 N-Butyl-N-methyl pyrrolidinium bis-(trifluoromethane sulfonyl)imide (NBNMPBTSI), which has low melting temperature, hydrophobic and highly cycleable properties within a wide voltage window, allowed hybrid ES to be operated

between 3.4 and 1.5 V. 1-Ethyl 3-methyl imidizolium bis-(trifluoromethylsulfonyl)imide showed better fluidity than NBNMPBTSI [20-22].

2.4.5 Comparison of EDLC and Pseudocapacitor [23]

Table 2.1: Comparison of EDLC and Pseudocapacitor Supercapacitors [21]

EDLC	**Pseudocapacitor**
Indefinitely reversible	Highly reversible
High-voltage operation	Low-voltage operation, limited by electrochemistry and decomposition voltage of solvent
Has state-of-charge self-indication	Has state-of-charge self-indication
Capacitance constant with voltage	Capacitance not constant with voltage

2.4.6 Fabrication and Manufacturing of Electrochemical Supercapacitor (ES)

Main processes in the fabrication of cells include five steps: (1) coating the electrode; (2) winding; (3) filling with an electrolyte; (4) testing; and (5) welding and sealing. The electrode, the heart of the cell, determines the ES performance in terms of self-discharge, life expectancy, capacity, resistance, and so on. Therefore, the electrode fabrication including an active material coating process is the most important step. As a result, stringently controlling the preparation process is necessary for achieving both durability high and performance. Normally, the charge collector is made from aluminium because of its high current-carrying capability, chemical stability and low cost. In the coating process of electrodes, firstly, binders, active materials and conductive additives are mixed to obtain a homogeneous slurry

with the desired density, and then the slurry is spread onto an etched aluminium foil, followed by drying the electrode and roll pressing to achieve a uniform electrode coating layer. Once the electrodes are prepared, they are brought into a glove box with ultra-low moisture. A pair of such electrodes, with a separator layer inserted between them, is wound around a central mandrel into the desired shape. Then the electrolyte is filled into this separator. The electrolyte-filling process generally requires special care. The amount of electrolyte in the cell is critical, because excess electrolyte can lead to excessive gassing and leakage in operation. Generally, the process is slow, typically taking one to two days, and is relatively labor intensive. This is because of the nanopore level of internal porosity of active materials, making the wetting process slow. After the completion of electrolyte filling, the cell is subjected to cycling test [20].

2.5 Cyclic voltammetry

The capacitance of a supercapacitor material can be assessed using cyclic voltammetry (cv) which is one of the commonest tools used. During CV testing, a varying electric potential which is linear is applied between positive and negative electrodes for two-electrode systems, or between reference and working electrodes for three-electrode configurations. The rate of the potential change in mVs^{-1} is designated as the sweep rate or scan rate, ν, and the range of potential change is called the potential window or operating potential. The instantaneous current during the cathodic and anodic sweeps is recorded to characterize the electrochemical reactions involved. The data are plotted as current (A*)* vs. potential (V*)* or sometimes as current (A*)* or potential (V*)* vs. time (s). The three-electrode setup is regarded as the most suitable approach to examine the charge storage mechanisms of supercapacitor (SC) materials [24].

2.6 Constant Current Charge/Discharge (CCCD)

Under direct current the most widely used method for the characterization of SCs is the CCCD testing. It is conducted by repetitive charging and discharging of the SC device or the working electrode at a constant current level with or without a dwelling period (a time period between charging and discharging while the peak voltage V_o remains constant), and normally the output is a plot of the potential (E) vs. time (s). Choosing a proper level of the constant current is critical to produce consistent and comparable data from a CCCD test. CCCD test is regarded as the most versatile and accurate approach in characterizing SC devices. All three core parameters of SC devices, C_T, R_{ES}, and V_o, can be tested from it and subsequently used to derive most of the other properties, such as the time constant, power and energy densities, and leakage and peak current. It can also be conveniently used to study the cycling stability of SC devices. Moreover, by using a three-electrode setup, the specific capacitance, reversibility, and potential window for SC materials can also be obtained via CCCD test [24].

2.7 Electrochemical Impedance Spectroscopy (EIS)

EIS testing, which is also known as the dielectric spectroscopic testing, measures the impedance of a power cell as a function of frequency by applying a low-amplitude alternating voltage (normally 5 mV) superimposed on a steady-state potential. The data that results from the test are usually expressed graphically in a Bode plot to demonstrate the cell response between the phase angle and frequency, and in a Nyquist plot to show the imaginary and real parts of the cell impedances on a complex plane. In addition to the frequency response and impedance, EIS has also been used to characterize the charge transfer, mass transport, and charge storage mechanisms, as well as to estimate the capacitance, energy, and power properties. To distinguish the contribution of individual structure component in a cell system to the total impedance, different equivalent circuits and models have been developed. The real

parts of the complex impedance at selected frequencies are used in literature to represent R_{ES} when SC devices are tested. However, one needs to remember that the R_{ES} from an EIS test is often much smaller than that derived from the CCCD test, and is as such, limited in describing the power performance of SC devices. The impedance, specific capacitance, charge transfer, mass transport, and charge storage of SC materials can be studied using EIS testing mechanisms. [24].

2.8 Equivalent Series Resistance

A SC is not an ideal electrical component in the sense that it has its own internal resistance, and thus dissipates the energy that is stored. A SC cell can be treated as a system of a capacitor in series arrangement with a resistor R_{ES}. The resistance of this resistor is usually called the equivalent series resistance, R_{ES}, and is essential in reflecting the power performance and energy efficiency of SCs. In general, a small R_{ES} is preferred for better electrochemical performance. R_{ES} is evaluated by analyzing the IR drop or voltage variation at the initial stage of the discharging curve from CCCD tests and by applying ohm's law to the IR drop, R_{ES} can be readily calculated:

$$R_{ES} = \frac{\Delta V}{\Delta I} \quad (1)$$

Where ΔV and ΔI are the voltage and current of the *IR* drop, respectively. A larger charge/discharge current used in the test will usually give rise to a smaller R_{ES}. If I is the constant current applied, then in the case of 0 min dwelling time the current change is [24].

$$\Delta I \cong 2I \quad (2)$$

2.9 Synthesis of Metal Oxides

There are many ways to synthesize metal nanoparticles and can be mainly divided into two categories: top down approach and bottom up approach. In the top down approach, the bulk materials are used as the starting materials and treated by physical means such as mechanical alloying, sputtering techniques and mechanical grinding to synthesize nanomaterials. The particles synthesized by this method generally have a broad size distribution. The metal nanoparticles synthesized by this method are typically larger and cannot be reproduced resulting in irreproducible catalytic activity. Single atoms or ions are allowed to grow into clusters or nanoparticles using wet chemical synthetic methods such as chemical reduction of metal salts, and the decomposition of precursors using thermal, sonochemical treatment in the bottom up process. The particles synthesized by this method have narrow size distribution of the particles. The method used for the synthesis of metal nanoparticles has control over the size and shape of the particles. Chemical synthesis methods are found to be more suitable methods to have better control over the particle size and shape, than physical synthesis. Chemical reduction of metal salts, thermal and photochemical decomposition of metal complexes and electrochemical reduction of metal salts are the three major routes used to synthesize transition metal nanoparticles. [25]

2.9.1 Chemical Reduction

One of the most widespread method used for the synthesis of transition metal nanoparticles is the chemical reduction of metal salts. In this method, the metal salts dissociate to form metal ions. The metal ions are then reduced by a reducing agent to form metal nanoparticles that are stabilized by a stabilizer. Most of the commonly used reducing agents include solvents such as sodium borohydride, alcohol, or sodium citrate and gases such as carbon monoxide and hydrogen. Ethanol, methanol and isopropanol are the alcohols mainly used for the reduction

of metal salts. The alcohols act both as a reducing agent and solvent. The transition metal nanoparticles are formed by the reduction of metal salts in the refluxing alcohol and the alcohols are oxidized to form corresponding carbonyl compounds (for example, methanol to formaldehyde, ethanol to acetaldehyde). The size distribution of the metal nanoparticles is dependent on the structure and quantity of the alcohol, the stabilizing agent, metallic precursor, temperature and the base used [26]. Borohydrides are the most commonly used reducing agents to synthesize colloidal transition metal nanoparticles. Sodium borohydride is dissolved in aqueous solution and used immediately to avoid decomposition of borohydride to borane and gaseous hydrogen that could escape from the solution. Sodium borohydride is also used as a reducing agent to synthesize platinum and palladium nanoparticles stabilized by PAMAM dendrimers. Sodium citrate is used as a reducing agent to synthesize Ir and Pt nanoparticles [27]. Turkevitch and co-workers [28] used sodium citrate as reducing agent to synthesize Au nanoparticles. The citrate anion acts both as a reducing agent and stabilizer. Larger size particles are produced as a result of the decrease in the amount of sodium citrate. The reduction in the amount of sodium citrate will result in less number of citrate ions available for stabilizing the particles and this causes the agglomeration of smaller particles to form bigger ones. Another commonly used reducing agent to synthesize colloidal transition metal nanoparticles is hydrogen gas. This method involves bubbling of hydrogen gas into a solution containing precursor metal salt and a slow reduction process allows the formation of colloidal metal nanoparticles. Hydrogen gas is used as a reducing agent to synthesize Ru, Pt, Ag, Pd, Ir, Rh and Au colloids in the presence of polyvinylalcohol. Polyphosphate is used as a stabilizer to synthesize Ag nanoparticles using hydrogen as reducing agent. Carbon monoxide is used as a reducing agent to synthesize Au nanoparticles in the presence of polyvinylsulfate [29] .

2.10 Synthesis of tin dioxide nanostructures

Many processes have been used to synthesize tin dioxide nanostructures, e.g., spray pyrolysis, conventional co-precipitation, and hydrothermal method: microwave assisted, reverse micelles and sol-gel method.

2.10.1 Hydrothermal Synthesis

Sir Roderick Murchison, a British geologist was the first to use the term 'hydrothermal' to describe the action of water at elevated temperature and pressure, in bringing about changes in the earth's crust leading to the formation of various rocks and minerals [30]. It is well known that the largest single crystal formed in nature (beryl crystal of >1000 g) and some of the large quantity of single crystals created by man in one experimental run (quartz crystals of several 1000s of g) are both of hydrothermal origin. Any heterogeneous reaction in the presence of aqueous solvents or mineralizers under high pressure and temperature conditions to dissolve and recrystallize (recover) materials that are relatively insoluble under ordinary conditions can be defined as hydrothermal processing [30]. Definition for the word hydrothermal has undergone several changes from the original Greek meaning of the words 'hydros' meaning water and 'thermos' meaning heat. Recently, Byrappa and Yoshimura define hydrothermal as any heterogeneous chemical reaction in the presence of a solvent (whether aqueous or non-aqueous) above the room temperature and at pressure greater than 1 atm in a closed system. However, there is still some confusion with regard to the very usage of the term hydrothermal. For example, chemists prefer to use a term, viz. solvothermal, meaning any chemical reaction in the presence of a non-aqueous solvent or solvent in supercritical or near supercritical conditions. Similarly, there are several other terms like glycothermal, alcothermal, ammonothermal, and so on. Further, the chemists working in the supercritical region dealing with the materials synthesis, extraction, degradation, treatment, alteration,

phase equilibria study, etc., prefer to use the term supercritical fluid technology. However, if we look into the history of hydrothermal research, the supercritical fluids were used to synthesize a variety of crystals and mineral species in the late 19th century and the early 20th century itself [24]. So, a majority of researchers now firmly believe that supercritical fluid technology is nothing but an extension of the hydrothermal technique. Hence, here authors use only the term hydrothermal throughout the text to describe all the heterogeneous chemical reactions taking place in a closed system in the presence of a solvent, whether it is aqueous or non-aqueous. The hydrothermal technique is among the various technologies available today in advanced materials processing, and it occupies a unique place owing to its advantages over conventional technologies. It covers processes like hydrothermal crystal growth leading to the preparation of fine to ultra- fine crystals, bulk single crystals, hydrothermal transformation, hydrothermal sintering, hydrothermal decomposition, hydrothermal stabilization of structures, hydrothermal dehydration, hydrothermal extraction, hydrothermal treatment, hydrothermal phase equilibria, hydrothermal electrochemical reactions, hydrothermal recycling, hydrothermal microwave supported reactions, hydrothermal mechanochemical, hydrothermal sonochemical, hydrothermal electrochemical processes, hydrothermal fabrication, hot pressing, hydrothermal metal reduction, hydrothermal leaching, hydrothermal corrosion, and hydrothermal synthesis [30].

In comparing with other techniques, hydrothermal synthesis generally has the advantage of:

- Low cost for equipment.
- A low temperature synthesis procedure.
- Composition and particle size control by changing preparation parameters [6].

Chin–Chang et al synthesize SnO_2 enriched Ru-Sn oxide composite via a two-step hydrothermal procedure which showed an excellent capacitive performances in H_2SO_4 as that for pure $RuO_2.xH_2O$ [6]. Mild hydrothermal conditions (material construction occurring

between 100 and 200 under autogenous pressures), have been applied to prepare various hydrous and crystalline transition metal oxides in the past few years, such as tungsten oxide, vanadium oxide, molybdenum oxide, titanium oxide, as well as lithium/sodium manganese oxides [18]. Lin Tan et al reported that Krishna and Komarneni [24] used both conventional-hydrothermal and microwave-hydrothermal methods to prepare SnO_2 nanoparticles of very high surface areas. The hydrothermal processing is an alternative to calcination for the crystallization of SnO_2 under mild temperature [10].

2.10.2 Instrumentation in hydrothermal processing of nanomaterials

A pressure vessel capable of containing a highly corrosive solvent at high temperature and pressure is required for material processing under hydrothermal conditions. Hydrothermal experimental investigators require facilities that must operate routinely and reliably under extreme pressure temperature conditions. Designing a suitable hydrothermal apparatus popularly known as an autoclave, or reactor, or pressure vessel, or high pressure bomb is the most difficult task to define, because each project has different objectives and tolerances. However, an ideal hydrothermal autoclave should have the following characteristics [23].

- Ease of assembly
- Inertness to acids, bases and oxidizing agents
- Sufficient length to obtain a desired temperature gradient.
- Leak-proof with unlimited capabilities to the required temperature and pressure range.
- Rugged enough to bear high pressure and temperature experiments for long periods with no damage so that no machining or treatment is needed after each experimental run.

The commonly used reactors in the hydrothermal processing of advanced nanomaterials are listed below [30]:

- Morey type e flat plate seal.
- General purpose autoclaves.
- Stirred reactors.
- TZM autoclaves.
- Cold-cone seal Tuttle-Roy type.
- Batch reactors.
- Flow reactors.
- Microwave hydrothermal reactors.
- Mechanochemical-hydrothermal.
- Piston cylinder apparatus.
- Belt apparatus.
- Opposed anvil.

2.10.3 Influence of Surfactants on particles

The term **surfactant** (short for ***surface-active-agent***) is used to describe a substance which exhibits some superficial or interfacial activity. It can be said that, when powders are prepared in presence of surfactants, CetylTrimethylammonium bromide **(**CTAB) as well as Dioctyl Sulfosuccinate sodium salt (AOT), the precipitated powders coated by a surfactant overlayer, the growth of powder is affected since the ions have to diffuse through the surfactant overlayer, which causes a reduction in grain growth. According to Jain et al [31] anionic surfactant AOT was more effective in reducing the grain growth as compared to the cationic surfactant CTAB [9], [31]. SnO_2 nanoparticles in the range of 8-13nm with different

morphologies were synthesized by Gnanam and Rajendran [10] using different surfactants. Therefore, the type of surfactant used, determines the morphology of the particles.

2.10.4 Microemulsion Synthesis method

Among all chemical methods the microemulsion has been demonstrated as a reproducible and a very versatile method that allows-control over the nanoparticle size, and yields nanoparticles with a narrow size distribution. In the macroscale microemulsions are homogeneous and in nanoscale are heterogeneous dispersion of two immiscible liquids consisting of nanosized domains of one or both liquids in the other, stabilized by an interfacial film of surface active molecules. Normal emulsion and microemulsion can be distinguished by their particle size and stability. Normal emulsions age by coalescence of droplets and Ostwald ripening. Microemulsions are thermodynamically stable, isotropic and usually form spontaneously. Microemulsions have ultralow interfacial tension, large interfacial area and capacity to solubilize both aqueous and oil-soluble compounds. Depending on the proportion of various components and hydrophilic–lypophilic balance (HLB) value of the used surfactant, microemulsions can be classified as water-in-oil (W/O), oil-in-water (O/W) and intermediate bicontinuous structural types that can turn reversibly from one type to the other. The dispersed phase consists of monodispersed droplets in the size range of 5 – 100 nm. The nanodroplet size can be modified by varying concerned parameters, e.g. the type of stabilizer, continuous phase, the precursor content dissolved within the nanodroplets, and the molar ratio of water to surfactant (*W*). In addition, the stability of the microemulsion can be influenced by addition of salt, concentration of reagents, temperature or pressure. The preparation procedure of metallic nanoparticles in W/O microemulsion commonly consists of mixing of two microemulsions containing metal salt and a reducing agent, respectively. After mixing two microemulsions, the exchange of reactants between micelles takes place during the collisions of water droplets, the attractive van der Waals forces and repulsive osmotic and elastic forces

between reverse micelles. Successful collisions lead to coalescence, fusion, and efficient mixing of the reactants. Metal nuclei are formed as a result of the reaction between solubilizates. A metal salt is reduced to give zero valent metal atoms in the initial stage of the nucleation, which then collides with further metal ions, metal atoms, or clusters to form an irreversible seed of stable metal nuclei. Growth then occurs around this nucleation point where successful collision occurs between a reverse micelle carrying a nucleus and another one carrying the product monomers with the arrival of more reactants due to intermicellar exchange. The nucleation reaction and particle growth take place within the micelles, and the size and morphology of as-prepared nanoparticles depend on the size and shape of the nanodroplets and the type of the surfactant, whose molecules are attached on the surface of the particles to stabilize and protect them against further growth [32-34].

Hui-Yuan Wang et al [29] prepared SnO_2 submicrospheres at ambient temperature with uniform morphology, high specific surface area and narrow size distributions, contributing to SnO_2 submicrostructures with large reversible capacity (846 $mAh \cdot g^{-1}$ after 50 cycles at a current density of 100 $mA \cdot g^{-1}$) and significantly improved cycling performance [35]. Song et al [30] synthesized nanoparticles of tin oxide (SnO_2) via water-in-oil microemulsions consisting of water, AOT (surfactant), and *n*-heptane (oil). Precursor hydroxides were precipitated in the aqueous cores of water-in-oil microemulsions and then calcined at 600°C for 2 hrs to form tin oxide powder. The formation of phase pure tin oxide was then confirmed by means of X-ray diffraction analysis. The tin oxide powder was found to be less than 40 nm in particle diameter and had a higher specific surface area, about 73 m^2/g, when compared with tin oxide powder prepared through the conventional precipitation method (19 m^2/g) [36].

2.11 Characterization Techniques

2.11.1 Scanning Electron Microscopy (SEM)

The object is scanned at the surface with the electron beam point by point whereby secondary electrons are set free. The angle of inclination of the object's surface determines the intensity of this secondary radiation. The signals that are derived from the electrons gives information about the sample including chemical composition, external morphology (texture) and crystalline structure and orientation of materials making up the sample. A detector that sits at an angle at the side above the object collects the secondary electrons. The signal is then enhanced electronically. The image appears on viewing screen and the magnification can be chosen depending on the model. An SEM machine is illustrated in Figure 2.5.

Figure 2.5: SEM Machine

2.11.2 X-Ray Diffraction (XRD)

Diffraction produced by the reticular planes that form from the atoms of the crystal is one of the phenomena of interaction of x-rays with crystalline matter. An x-ray beam passing through a crystal will be diffracted at specific angles depending on the x-ray wavelength, the crystal orientation and the structure of the crystal. In the macroscopic version of x-ray diffraction, a certain wavelength of radiation will constructively interfere when partially reflected between surfaces (i.e., the atomic planes) that produce a path difference equal to an integral number of wavelengths. This condition is described by the Bragg law:

$$2d \sin \theta = n\lambda \qquad (3)$$

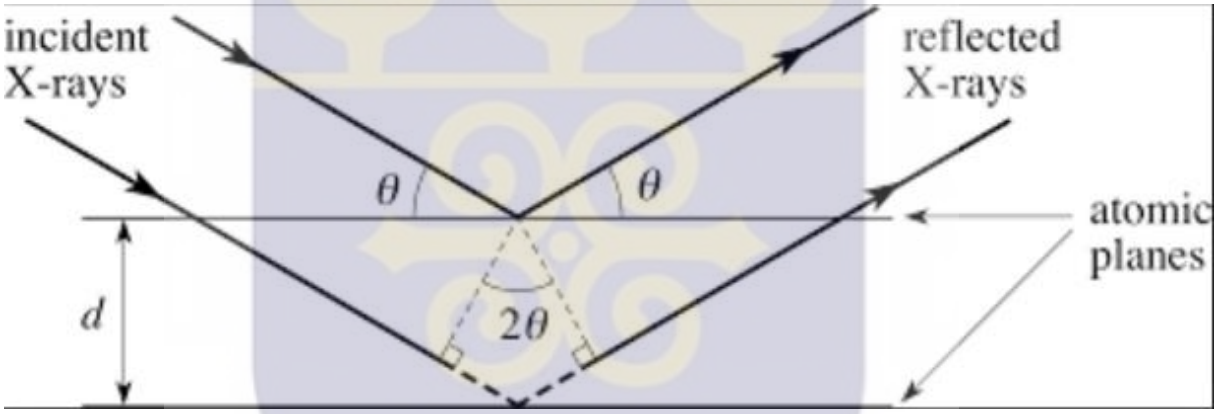

Figure 2.6: Illustration of the Bragg's law

where n is an integer, λ is the wavelength of the radiation, d is the spacing between surfaces and θ is the angle between the incident beam of radiation and the atomic plane. This relation reveals that interference effects are observable only when radiation interacts with physical dimensions that are approximately the same order of magnitude as the wavelength of the radiation. Diffraction methods to characterize materials require radiation in the x-ray region of the electromagnetic spectrum, or beams of electrons or neutrons with similar wavelength, since the distances between atoms or ions in a substance are on the order of 1 Å. Therefore, through x-ray diffraction spectra one can identify and analyze any crystalline material. An x-

ray diffractometer basically, consists of an x-ray generator, a goniometer and sample holder and an x-ray detector, such as photographic film or a movable proportional counter. X-ray tubes, which generate x-rays by bombarding a metal target with high energy (10-100 keV) electrons that knock out core electrons are the most usually employed instrument to generate x-rays. Thus, an electron in an outer shell fills the hole in the inner shell and emits an x-ray photon. Mo and Cu, which have strong K X-ray emissions at 0.71073 and 1.5418 Å, respectively are the two common targets used. Aside these spectral lines, other accompanying lines appear, which have to be eliminated in order to monochromatize the x-rays to enable the interpretation of the spectra. Crystal monochromators are used to partially suppress these lines. Powder cameras or powder diffractometers can be used to acquire powder diffraction patterns experimentally. Powder camera is the simplest instrument and many factors can contribute to the decision to select a camera technique rather than a powder diffractometer. These factors include the desire of maximum resolution, the lack of adequate sample quantity, and the lower initial cost. Of the various camera types the Debye-Scherrer camera is the most usually used, probably because it is the simplest and easiest to use. In it, the sample itself can be packed in a glass capillary or, if very small sized sample, mounted on the tip of a glass rod or other rigid material using rubber cement or other permanent adhesive. The sample is placed at the camera center and aligned to the incident beam. The diffracted beams intensities are proportional to the crystalline sample volume irradiated by the beam. Thus, times for exposure have to be increased as the sample size decreases. In the Debye Scherrer powder camera the whole diffraction pattern is recorded simultaneously. Diffractometer data are generally of good quality than Debye-Scherrer data, mainly because the shapes of the lines (or peaks) of Debye-Scherrer data are affected by both the adsorption of the specimen and the physical size of the specimen.

The photographic film (or some annular detector) used in cameras in powder diffractometers are replaced with a photon detector. The majority of commercially available powder diffractometers use the Bragg-Brentano parafocusing arrangement. A given instrument may provide a horizontal or vertical θ/2θ configuration or a vertical θ/θ configuration. In it, all the rays diffracted by suitably oriented crystallites in the specimen at an angle 2θ converge to a line at the receiving slit. A radiation detector, usually a scintillation counter or a sealed gas proportional counter is used to detect the x-rays. The receiving slit assembly and the detector are coupled together and move around a circle in order to scan a range of 2 (Bragg) angles. For θ/2θ scans, the specimen is rotated about the same axis by the goniometer as the detector but at half the rotational speed. The surface of the specimen therefore remains tangential to the focusing circle. The goniometer which acts as a support for all of the various slits and other components which make up the diffractometer, also sets the angles θ and 2θ. The parallel-plate collimators serves the purpose of limiting the axial divergence of the beam and thus partially control the shape of the diffracted line profile. It follows that the center of the specimen surface must be on the axis of the goniometer and this axis must be also parallel to the axis of the line focus, divergence slit and receiving slit [12]. The designation for its identification of each crystalline solid is given by its x-ray diffraction pattern. XRD may be used to determine its structure, i.e. how the atoms pack together in the crystalline state and what the interatomic distance and angle are etc. From these points it can be concluded that x-ray diffraction has become a very important and powerful tool for the structural characterization in solid state physics and materials science. Figure 2.7 shows the setup for a typical XRD machine.

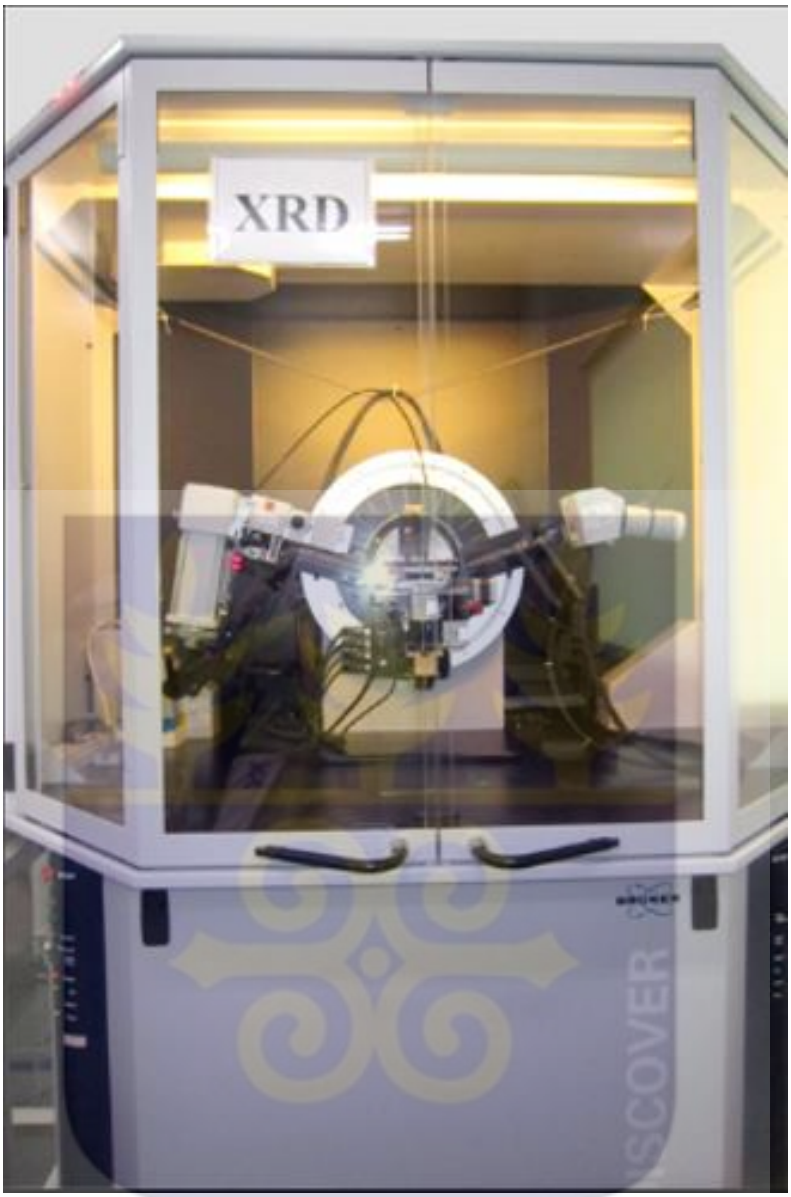

Figure 2.7: XRD Machine

CHAPTER THREE

3.0 Experimental Design

This chapter gives a precise description of the procedures, methods, materials, tools and equipment used in obtaining the results.

3.1 Materials

Chemicals used in this study, their purity and sources of procurement are listed below:

- Tin Chloride pentahydrate ($Sncl_4.5H_2O$), 98% Sigma Aldrich,
- Urea ($CO(NH_2)_2$), Paskem;
- Soduim Borohydride ($NaBH_4$), Lab. Tech chemicals; Sodium Hydroxide (NaOH), n-hexane ($CH_3(CH_2)_4CH_3$), 95% Sure Chem. products Ltd.; Ethanol (C_2H_5OH), 96%, BDH laboratory supplies (Analar); distilled water; Dioctyl Sulfosuccinate sodium salt (AOT, $C_{20}H_{37}NaO_7S$), Sigma Aldrich; Cetyl Trimethyl ammonium bromide (CTAB, $C_{19}H_{42}BrN$), Central Drug House Ltd.

3.2 Equipment

The analytical tools and equipment used include:

- Autolab PGSTAT205 (Metrhom BV),
- XPERT-PRO diffractometer (PANalytical BV, Netherlands)
- Zeiss Ultra plus 55 field emission scanning electron microscope
- Vertex 70v (Bruker) spectrometer

3.3 Synthesis of SnO_2 Nanoparticles

The SnO_2 nanoparticles were synthesized using the water-in-oil microemulsion and hydrothermal techniques.

3.3.1 Water- In – Oil (reverse micelle) Microemulsion Synthesis of SnO_2 particles

3.254 g of AOT was added to a solution consisting of 62 ml hexane and 62 ml of Isopropanol. The mixture was then stirred at a rate of 125 rpm until the AOT was completely dissolved. 8 ml of $SnCl_4.5H_2O$ (0.2 M) was then added to the above mixture and stirred to obtain a homogeneous mixture after which 0.548 ml of NaOH (1 M) was added drop-wise. The colloid was then stirred at a steady rate of 125 rpm for 30 mins to allow time for the SnO_2 particles to form.

10 ml of acetone was then added to the colloid in order to break the surface tension for the as-synthesized particles to settle. The as-synthesized particles were washed with water and ethanol in a ratio 1:1 via centrifugation several times to get rid of any impurity that might be present and dried at 100°C overnight. The as-obtained particles were then calcined at 600°C for 3 hours after which they were characterized using X-Ray Diffraction, Scanning Electron Microscope, Energy Dispersive X-ray, Brunner Emmet Teller, Fourier Transform Infrared and UV-visible Spectroscopy. The samples prepared by the water-in-oil microemulsion were designated as ‘E’.

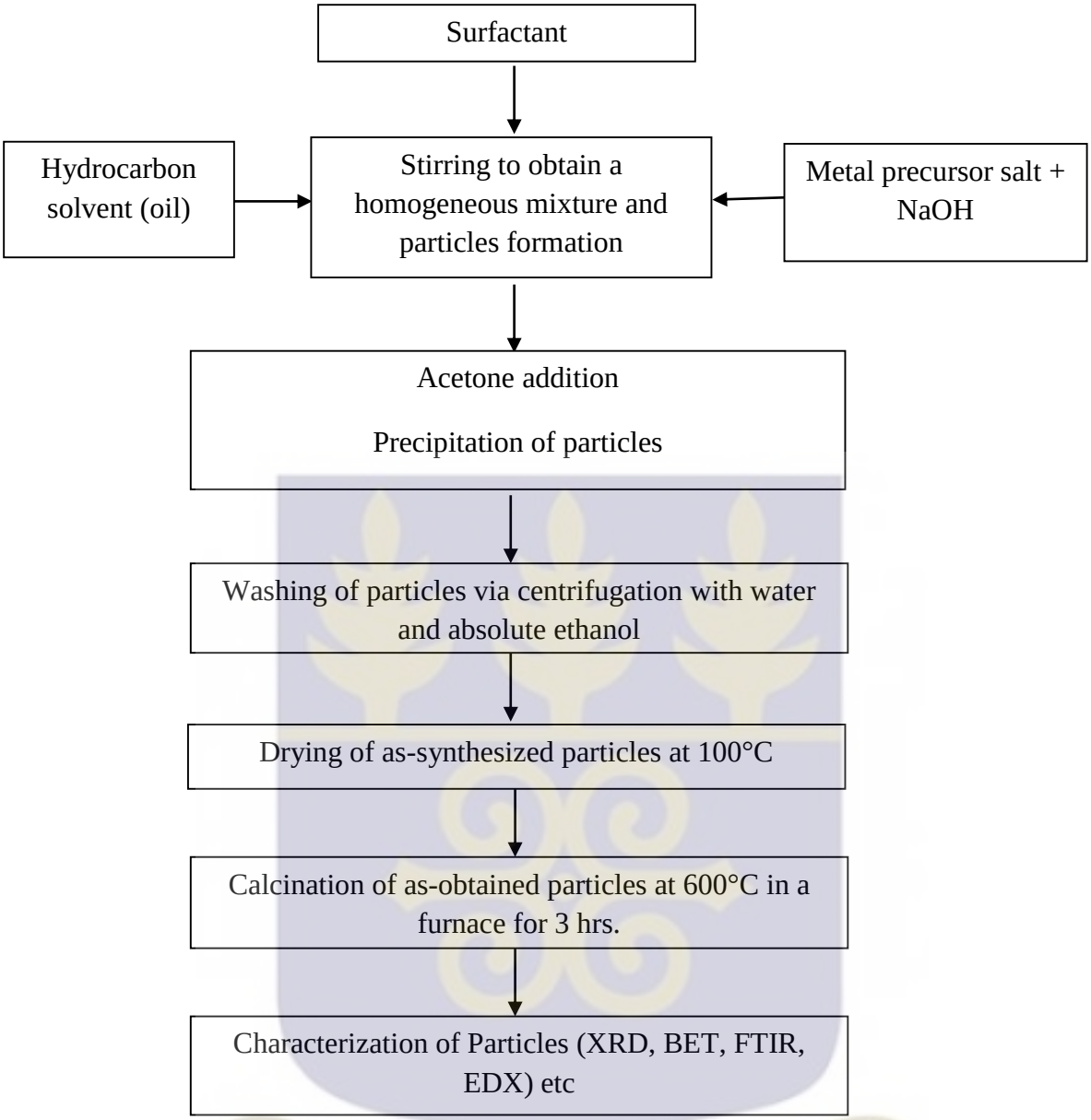

Figure 3.1: The process flow chart used for synthesis of nanosized SnO_2 powders by the reverse micelle microemulsion synthesis technique.

3.3.2 Hydrothermal Synthesis

For the hydrothermal synthesis of SnO_2 nanoparticles, two reducing agents (Urea and Sodium Borohydride, a cationic (CTAB) and anionic (AOT) surfactants were used. In a typical synthesis, 2.6 g of urea was added to a solution consisting of 60 ml of water and 60 ml ethanol whiles stirring. The mixture was then rigorously stirred for 15 mins after which it was

autoclaved at 120°C for 7 hours for complete reaction to take place. The reaction mechanism is represented by the Equations 4 to 8. After autoclaving, the precipitates from the precursor solution were washed several times with water and ethanol via a centrifuge to rid the precipitates of any impurity. The washed precipitates were then dried in an oven at 100°C overnight after which the dried precipitates were then calcined in a furnace at 600°C for 3 hrs. The final product was characterized using X-Ray Diffraction, Energy Dispersive X-ray, Scanning Electron Microscope, Fourier Transform Infrared spectroscopy and Bruner Emmet Teller. The same procedure was repeated for the other samples. The flow chart for the synthesis process is presented in Figure 3.2.

Reaction equation for precursor solution using urea

$$CO(NH_2)_{2(s)} + H_2O \rightarrow CO_{2(g)} + 2NH_4^+ + 2OH^- \quad (4)$$

$$Sn^{4+} + 4OH^- \rightarrow Sn(OH)_4 \quad (5)$$

$$Sn(OH)_4 \xrightarrow{heat} SnO_2 + 2H_2O \quad (6)$$

Reaction equation for precursor solution using Sodium Borohydride

$$SnCl_{4(s)} + NaBH_{4(s)} \rightarrow NaCl_{(s)} + Sn(BH_4)_{4(s)} \quad (7)$$

$$Sn(BH_4)_{4(s)} + H_2O_{(l)} \rightarrow Sn(OH)_{4(s)} + BH_4 \quad (8)$$

$$Sn(OH)_{4(s)} \xrightarrow{heat} SnO_{2(s)} + 2H_2O_{(g)} \quad (9)$$

Table 3.1: Sample groups and designation for the hydrothermal synthesis

Sample ID	$SnCl_2.2H_2O$	Reducing Agent	Surfactant
A	2.1g $SnCl_2.2H_2O$	2.6g Sodium Borohydride	-
AA	2.1g $SnCl_2.2H_2O$	2.6g Sodium Borohydride	2.0 g AOT
AT	2.1 g $SnCl_2.2H_2O$	2.6 g Sodium Borohydride	2.0 g CTAB
C	2.1 g $SnCl_2.2H_2O$	2.6 g Urea	-
CA	2.1 g $SnCl_2.2H_2O$	2.6 g Urea	2.0 g AOT
CT	2.1 g $SnCl_2.2H_2O$	2.6 g Urea	2.0 g CTAB

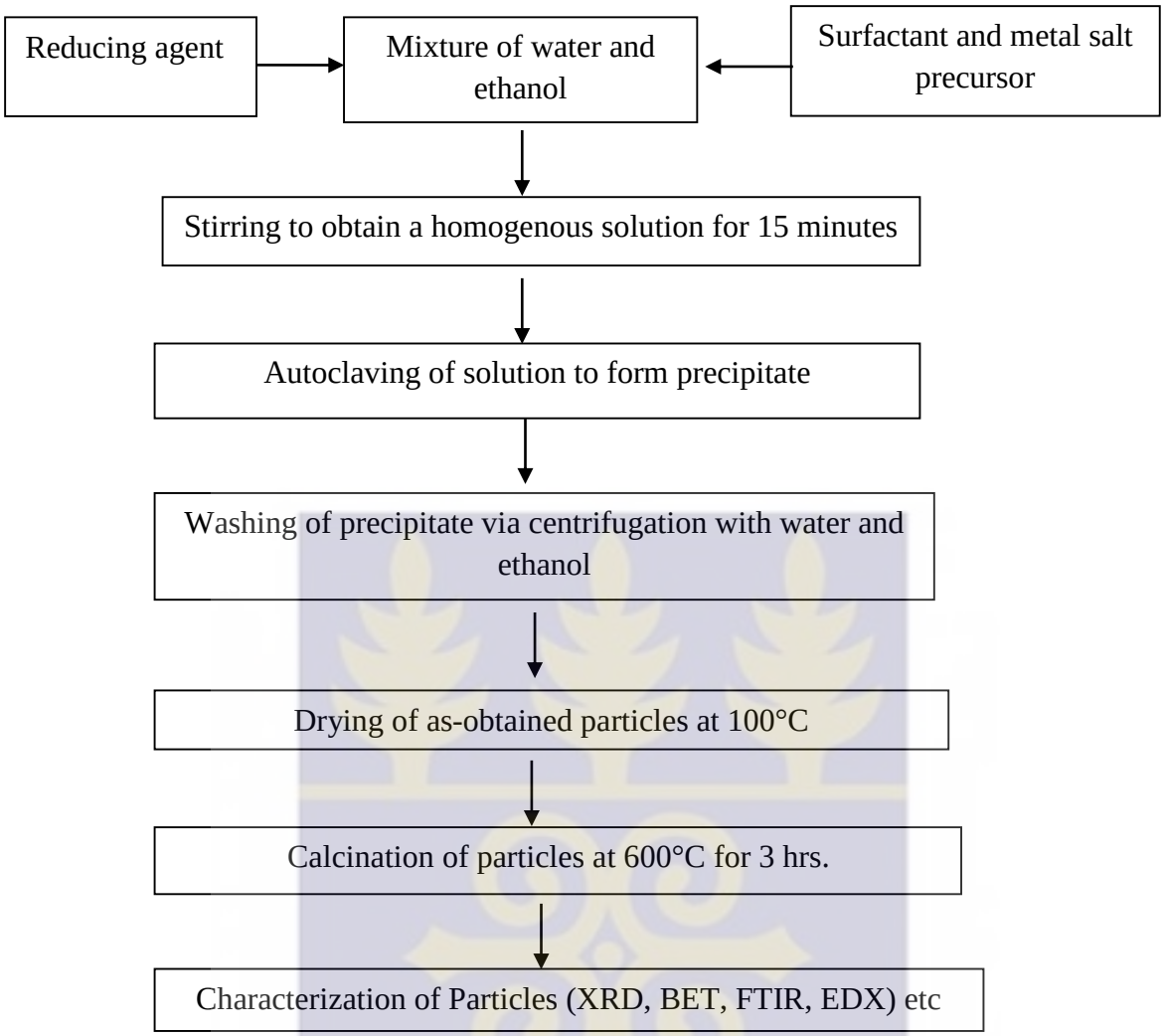

Figure 3.2: The process flow chart used for synthesis of nanosized SnO_2 powders by hydrothermal synthesis.

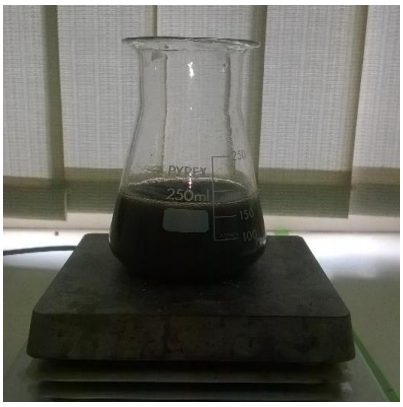

(a)Dissolution process for SnO_2 particle formation

(b) Autoclaving

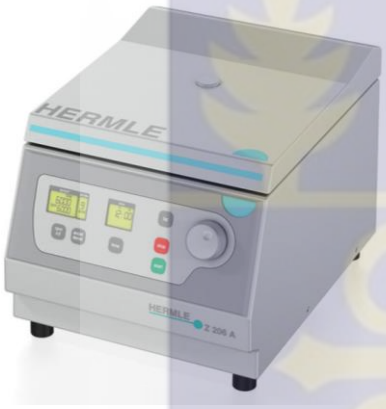

(c)Washing of as-synthesized particles via a centrifuge

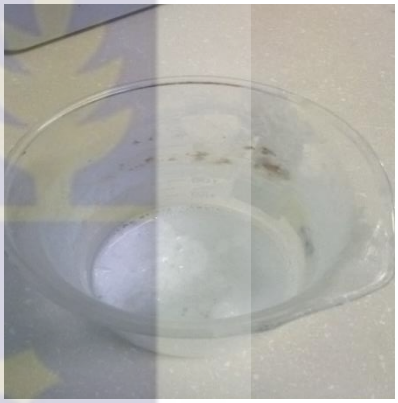

(d) as-synthesized SnO_2

(e) Drying of the as-synthesized particles

(f) Calcination of as-synthesized particles

Figure 3.3: Synthesis process of SnO_2 particles

3.4 Chemical characterization of SnO_2 nanoparticles.

3.4.1 X-Ray Diffraction

Figure 3.4: Panalytical Empyrean X-ray Diffractometer

To determine the phases present and the microstructure of the SnO_2 nanoparticles, X-ray powder diffraction (XRD) patterns were collected on an Empyrean diffractometer (Panalytical BV, Netherlands) in Figure 3.4 with theta/theta geometry, operating Cu Kα radiation tube (λ = 1.5418 Å) at 40 kV and 45 mA. The XRD patterns of all the randomly oriented powder specimens were recorded in the 20°- 70° 2θ range with a step size of 0.017° and a counting time of 14 s per step. The diffraction patterns were matched against the ICSD's PDF database and qualitative phase analysis conducted using the X'Pert Highscore plus search match software (Panalytical, Netherlands). The instrumental resolution function was characterized with the NIST SRM 640d (Si) standard [37] and all peak profiles were simultaneously fitted

with symmetrical pseudo-Voigt functions whose width and shape were constrained according to the Caglioti et al. formulae [38]. Microstructural analysis was performed using the Whole Powder Pattern Modelling (WPPM) method [39], with the aid of the PM2K software [40].

3.4.2 Scanning Electron Microscopy (SEM)

A high resolution Zeiss Ultra plus 55 field emission scanning electron microscope (FESEM) operated at 2.0 KV was used in the surface morphological investigations of the as-produced particles.

Figure 3.5: Zeiss ultraplus FESEM

3.4.3 Fourier Transform Infrared (FTIR) Spectroscopy

Transmission FTIR spectra were recorded on a Vertex 70v (Bruker) spectrometer in the 4000-400 cm^{-1} range with 4 cm^{-1} resolution. Sample compartment was evacuated during acquisition and the contact between the sample and the diamond ATR crystal is 2 mm diameter. Spectra were recorded and analyzed with the Opus software.

Figure 3.6: Vertex 70v (Bruker) FTIR spectrometer

3.5 Preparation and Electrochemical Characterization of SnO_2 Electrodes

3.5.1 Pretreatment of the Ni foam substrate

The Ni foam substrate was carefully etched with hydrochloric acid (HCl 2 M) for thirty minutes to ensure the removal of NiO layer on the surface. The etched Ni substrate was then rinsed in ethanol and distilled water severally via an ultrasonic cleaner.

3.5.2 Preparation of the SnO_2 Working Electrodes.

The working electrode for electrochemical evaluation were prepared by mixing 98 wt% of SnO_2 nanoparticles from the various treatments and 2 wt% polyvinylidene difluoride (PVdF) binder in a mortar. The mixture was then dissolved in 1-methyl-2-pyrrolidinone (NMP) to form a slurry. The slurry was coated on the treated Ni foam with dimensions 3 cm x 1 cm and pore size of 450 µm and dried at 80°C overnight to ensure complete evaporation of the NMP. Figure 3.7 illustrate the SnO_2 particles electrode making process.

3.5.3 Characterization of the Electrodes

The electrochemical test of the SnO_2 electrodes was performed in a three electrode configuration using glassy carbon rod as counter electrode and Ag/AgCl (3 M KCl) as the reference electrode in 1 M KOH electrolyte. The electrochemical properties of the supercapacitor were studied using cyclic voltammetry (CV), Chrono potentiostat charge-discharge and electrochemical impedance spectroscopy (EIS) using Autolab PGSTAT workstation 101 driven by the NOVA software.

The CV tests were carried out in the potential range of 0 to 0.5 V at different scan rates ranging from 5 mV/s to 100 mV/s. the EIS measurements were performed in the frequency range of 100 kHz-10 mHz. The EIS data were analyzed using Nyquist plots in Figure 4.18.

(a) Mixing of particles with PVdF binder

(b) Coating of slurry on the Ni substrate

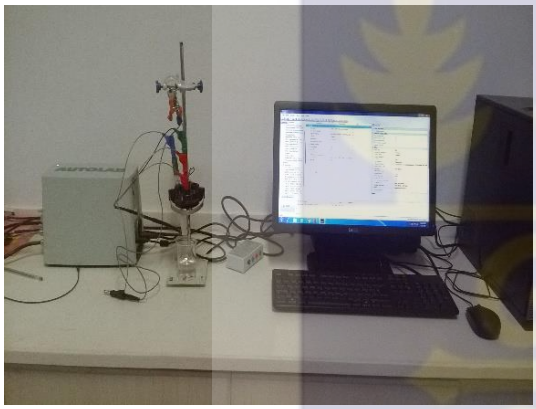

(c) Electrochemical measurement setup

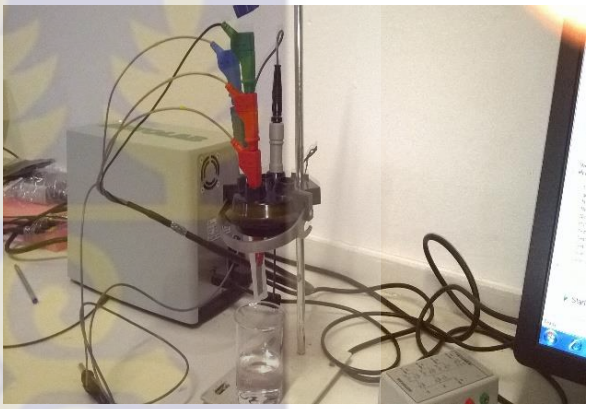

(d) SnO_2 working electrode

Figure 3.7: SnO_2 electrode making and electrochemical testing process

CHAPTER FOUR

4.0 Results and Discussions

4.1 pH of Precursor Solutions

The pH of the precursor solutions were measured with a pH meter and recorded in Table 4.1.

Table 4.1: pH of precursor solutions for as-synthesized SnO_2 nanoparticles by different treatments.

Sample Id	Method	pH
A	$SnCl_2.2H_2O$ + Sodium Borohydride	9.03
AA	$SnCl_2.2H_2O$ + Sodium Borohydride + AOT	9.18
AT	$SnCl_2.2H_2O$ + Sodium Borohydride + CTAB	8.94
C	$SnCl_2.2H_2O$ + Urea	8.27
CA	$SnCl_2.2H_2O$ + Urea + AOT	8.42
CT	$SnCl_2.2H_2O$ + Urea + CTAB	8.12

From the Table 4.1 it can be seen that when sodium borohydride was used as the reducing agent (samples A, AA, AT), the pH was higher than when urea was used as the reducing agent (samples C, CA, CT). It can also be observed that, the addition of CTAB to both sodium borohydride and urea precursor solutions (samples AT, CT) decreased the pH and this could be attributed to the fact that, CTAB in aqueous solution dissociate to produce NH_4^+ ions

which consumes OH^- ions in the aqueous medium. Hence, there is OH^- deficiency and more H^+ in solution, therefore there is decrease in pH. The addition of AOT (Samples AA, CA) tends to increase the pH and this is because, in aqueous medium AOT dissociates to produce SO_7^- ions which consumes the H^+ ions in solution hence increasing the OH^- ions and pH.

4.2 X-Ray Diffraction Analysis

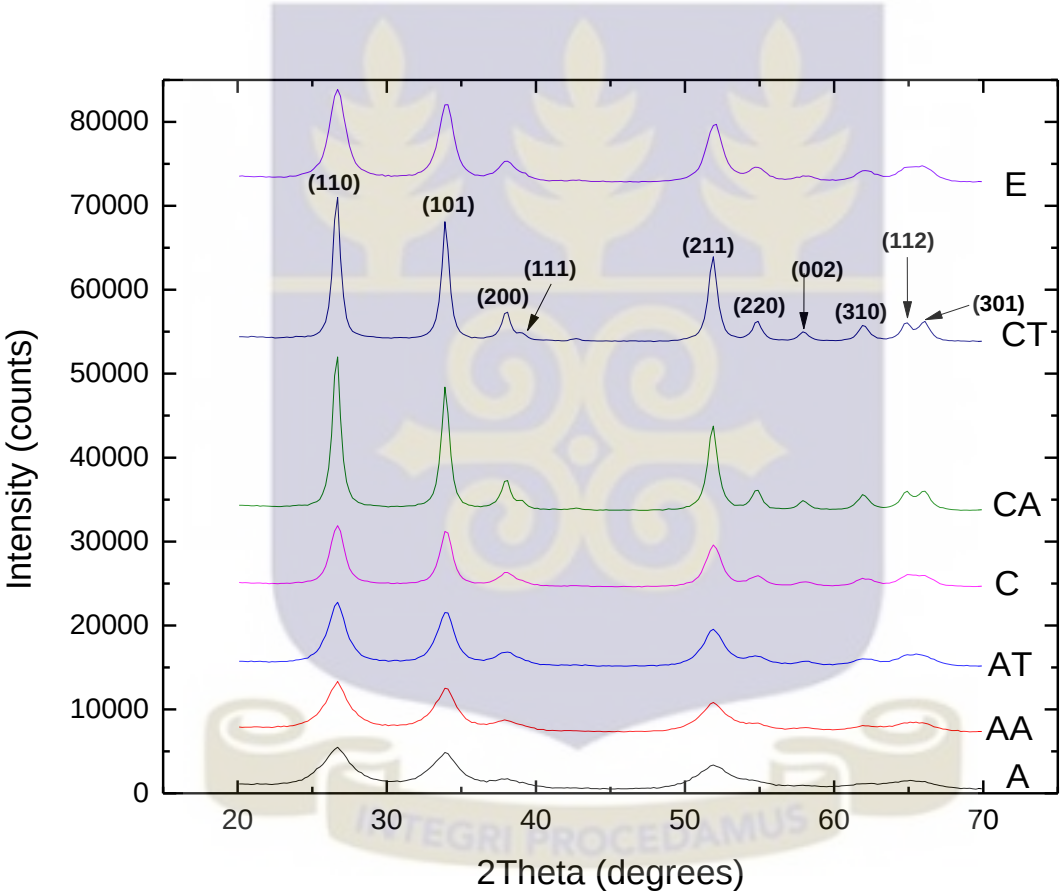

Figure 4.1: XRD patterns of SnO_2 nanoparticles

The diffraction peaks in Figure 4.1 are markedly broadened, which indicate that the crystalline sizes of samples are very small with the average size estimated from Figure 4.2 being 2.1 nm, 2.2 nm,5.0 nm, 4.0 nm, 9.5 nm and 8.6 nm for A, AA, AT, CA, C and CT respectively. It can be seen from the XRD data that samples produced with sodium borohydride (A, AA and AT) have broader and less intense peaks than samples produced with

urea (C, CA and CT) which means that the samples produced with sodium borohydride have smaller crystallite sizes than particles produced with urea. This can be attributed to the fact that samples produced with sodium borohydride have higher pH than samples produced with urea and the higher the pH, the smaller the particles sizes [41]. In a higher pH value solutions, the coordinated water molecules suppress the agglomeration among the freshly formed nanocrystallites [41, 42]. Whole Powder Pattern Modelling (WPPM) approach using the PM2K software which connects a physical model for the microstructure with the diffraction pattern, allowing an extraction of the microstructure parameters without recurring arbitrary peak shapes to fit each diffraction peak was used for the microstructure analysis. A typical diffraction pattern of sample CT modelled with the WPPM is shown in Figure 4.2. The modelling was carried out by assuming the presence of a lognormal distribution (figure 4.3) of aligned spherical domains. The almost featureless nature of the residual line in Figure 4.2 indicates a good agreement between experimental data and model which also suggests that the shape assumption is right for the domains investigated.

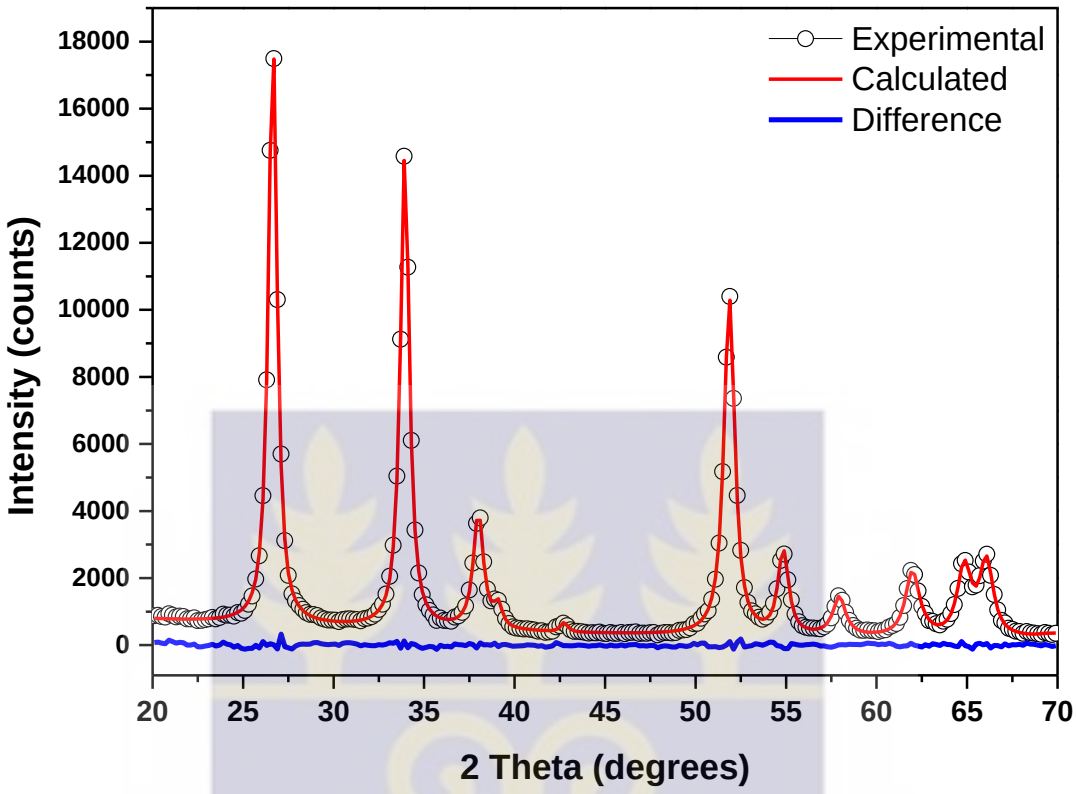

Figure 4.2: SnO_2-CT modelled using WPPM

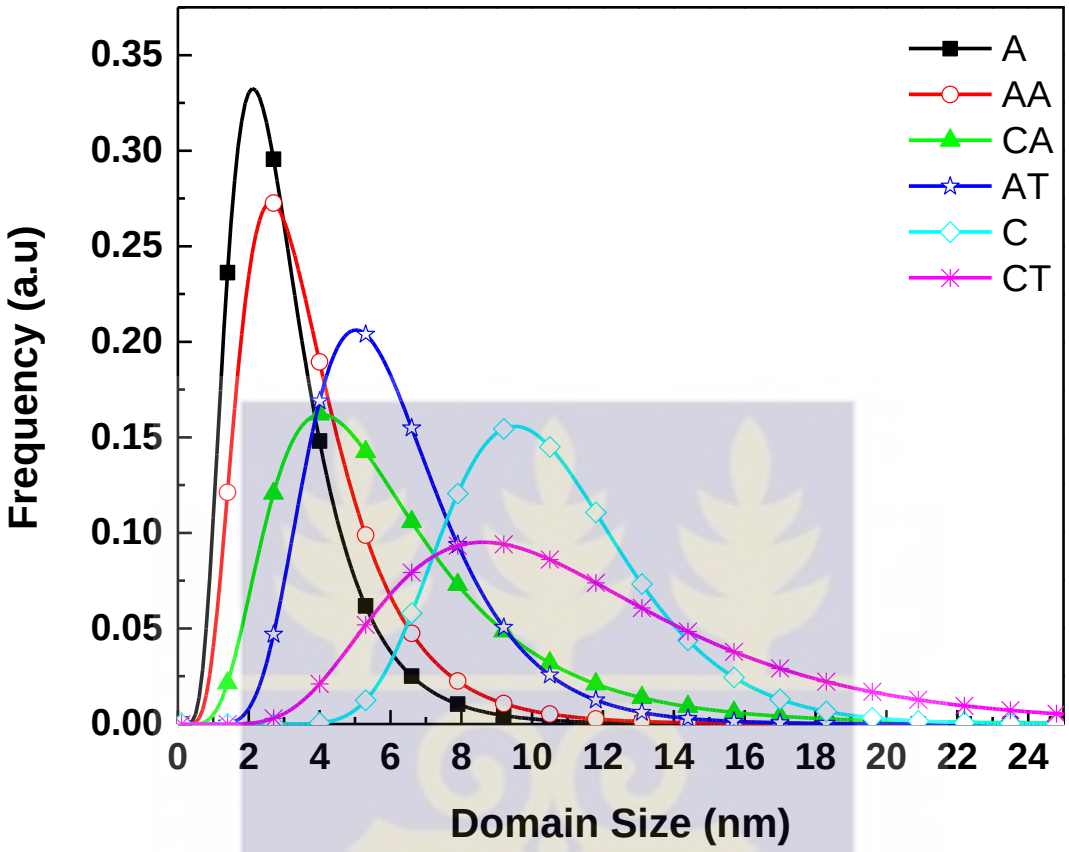

Figure 4.3: Lognormal Size Distribution Analysis of the SnO_2 particles

4.3 Fourier Transform Infra-Red Spectroscopy (FTIR)

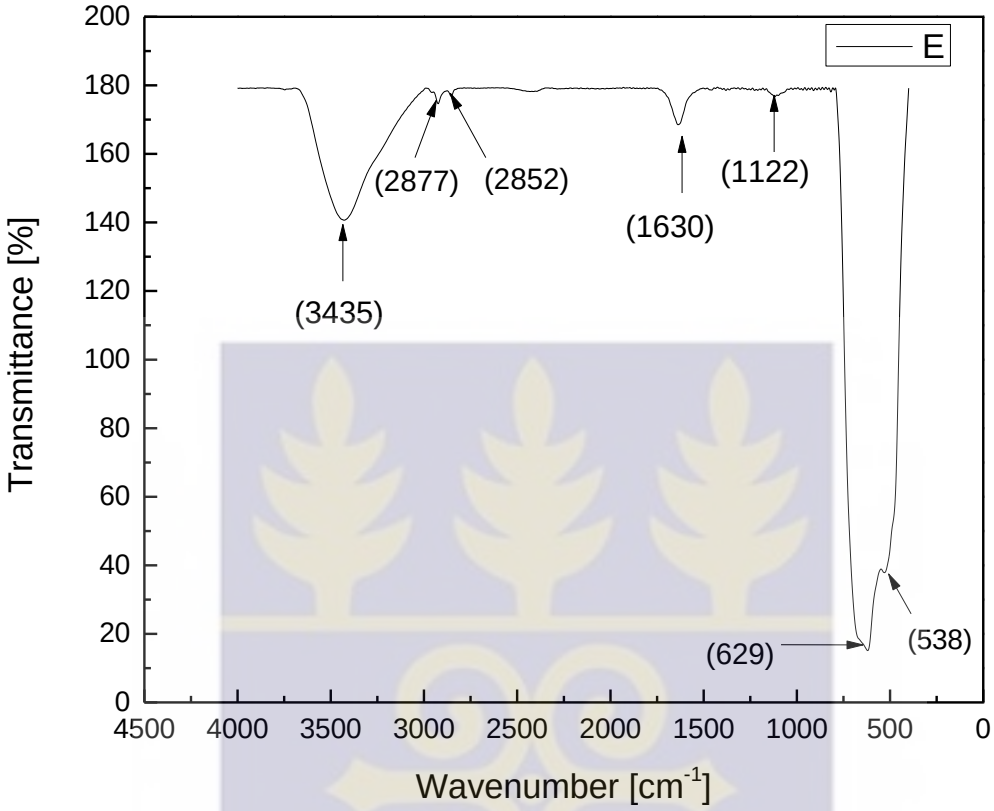

Figure 4.4: FTIR for the water-in-oil microemulsion synthesis (E) of SnO_2 nanoparticles

The peaks occurring at about 1122 cm^{-1}, 629 $cm^{-1}$and 538 cm^{-1}in Figure 4.4 are attributed to Sn–O stretching modes of Sn–O–Sn and Sn–OH [43]. The peak at about 1630 cm^{-1} belongs to H-OH bonds coming from the moisture content of the powder and the peak at 3435 cm^{-1} is attributed to Sn-OH bonds [44]. Peaks at 2877 and 2852 cm^{-1} can also be attributed to hydroxyl groups that are absorbed on the Tin Oxide surface. There are no impurity peaks from the surfactant used, which together with the XRD data confirm that phase pure SnO_2 nanoparticles were synthesized using the water-in oil microemulsions technique.

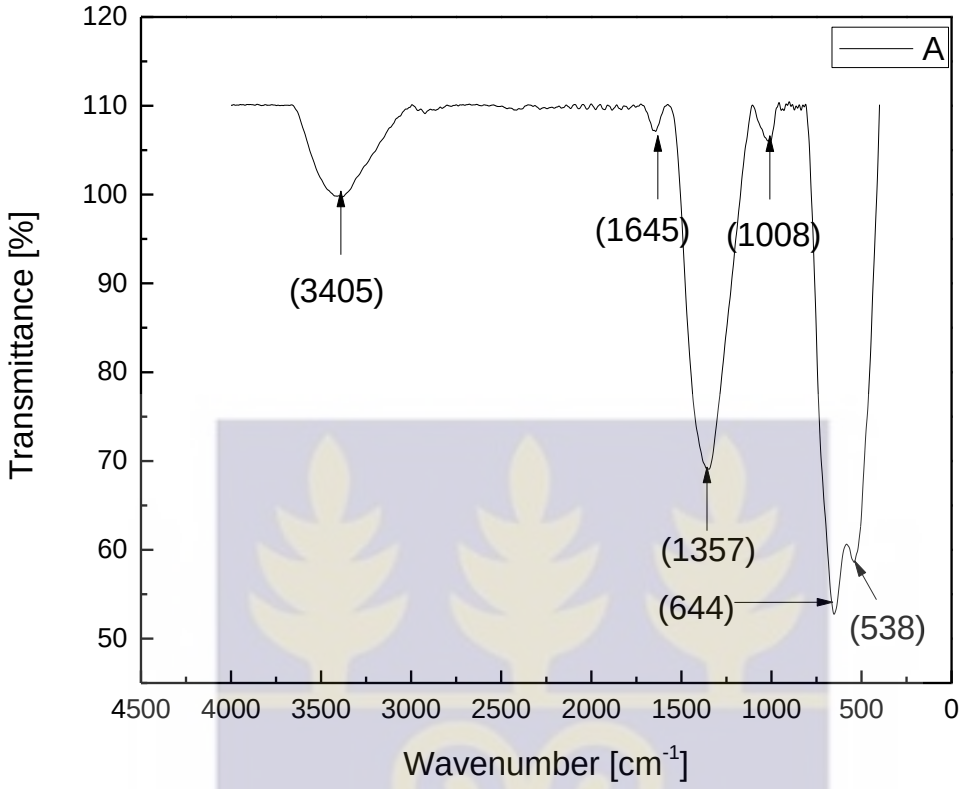

Figure 4.5: FTIR spectra of SnO_2 nanoparticles with sodium borohydride as the reducing agent (A).

Figure 4.5 represents the FTIR spectra of SnO_2 particles prepared using sodium borohydride as a reducing agent. The peak at 3405 cm^{-1} is attributed to Sn-OH bonds. Peaks at 1008 cm^{-1}, 644 cm^{-1} and 538 cm^{-1} are attributed to Sn–O stretching modes of Sn–O–Sn and Sn–OH. Peak at 1645 $cm^{-1}$and 1357 cm^{-1} are attributed to H-OH bonds coming from the moisture content of the powder and Sn-OH bonds respectively.

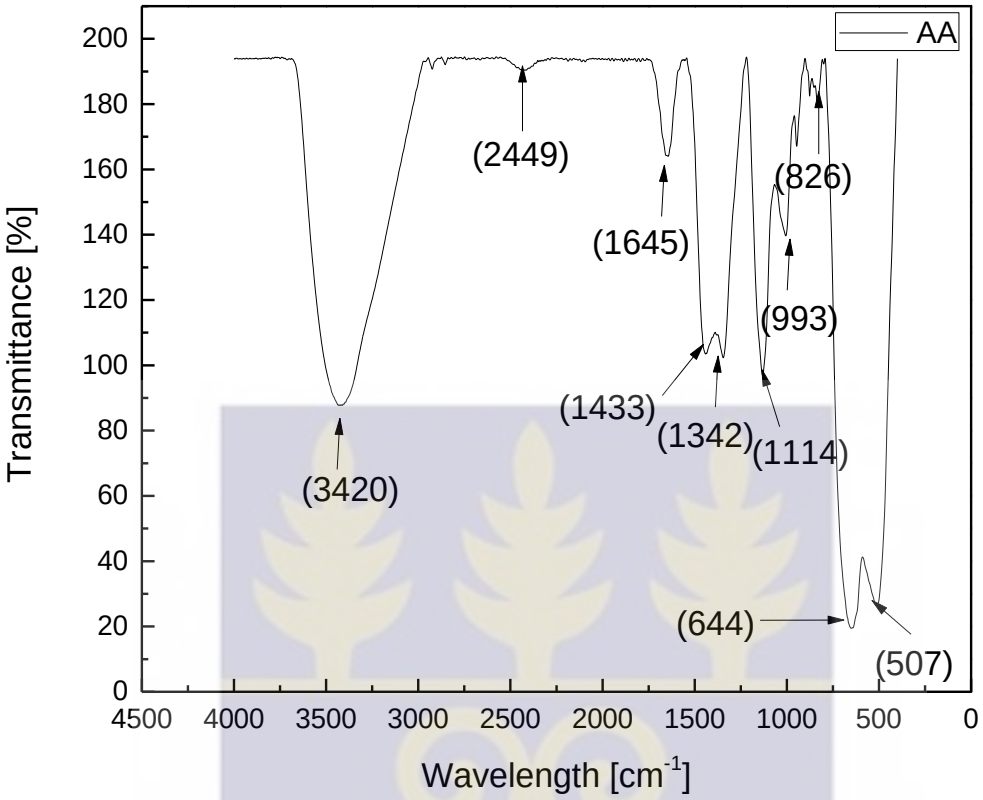

Figure 4.6: FTIR spectra of SnO_2 nanoparticles with sodium borohydride as the reducing agent and AOT as the surfactant (AA)

The hydrophobic group R-SO_3 Na^+ of AOT is responsible for the peak at 993 cm^{-1} and 1114 cm^{-1}. From the above result (figure 4.6), it is obvious that AOT molecules are adsorbed in the pores of the powders [45]. 2449 cm^{-1} , 3420 cm^{-1} and 1342 cm^{-1} peaks are attributed to Sn-OH bonds [44]. Peak at 1645 cm^{-1} is also assigned to H-OH bonds from the moisture content of the powder. 1433 cm^{-1} peak corresponds to bending vibrations of $–CH_2$. Which shows that a few organic groups are absorbed on the surfaces of SnO_2 nanoparticles [31] which could be as a result of combustion of the organic groups.

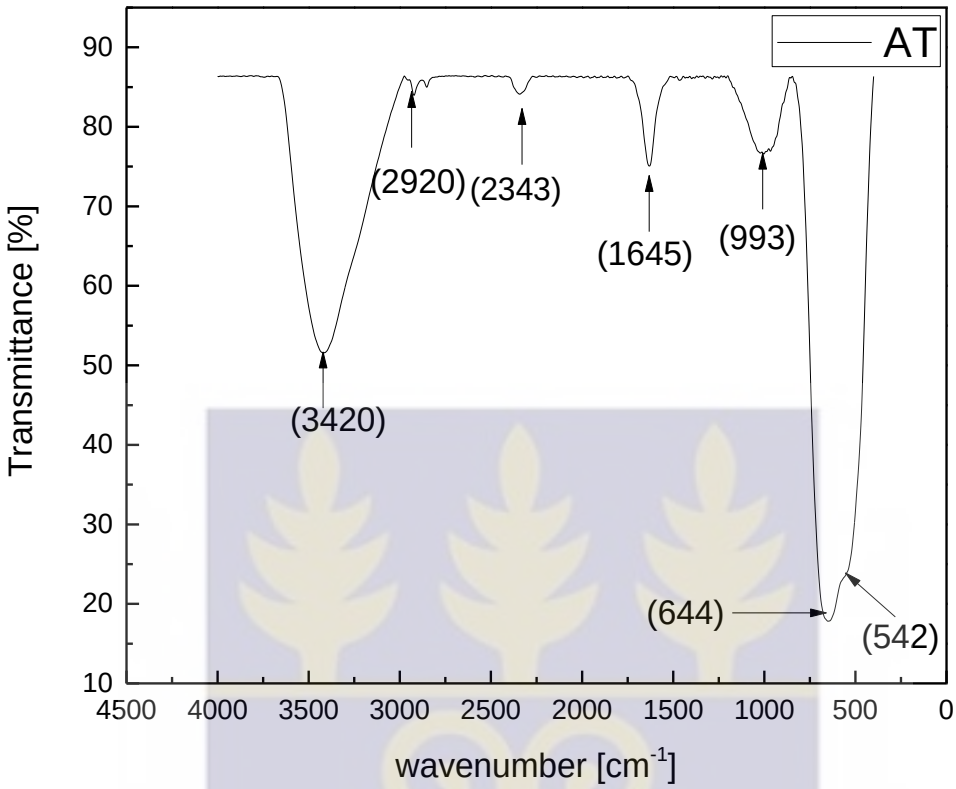

Figure 4.7: FTIR spectra of SnO_2 nanoparticles with sodium borohydride as the reducing agent and CTAB as the surfactant (AT).

From the Figure 4.7, the peak at 2920 cm^{-1} can be attributed to CH stretching [10]. The peak at 3420 cm^{-1}, 1645 cm^{-1}, and 993 cm^{-1} are assigned to Sn-OH bonds, H-OH bonds from the moisture content of the powder and the hydrophobic group R-SO_3 Na^+ of AOT respectively [45]. 644 cm^{-1} 542 cm^{-1} peaks are attributed to Sn–O stretching modes of Sn–O–Sn.

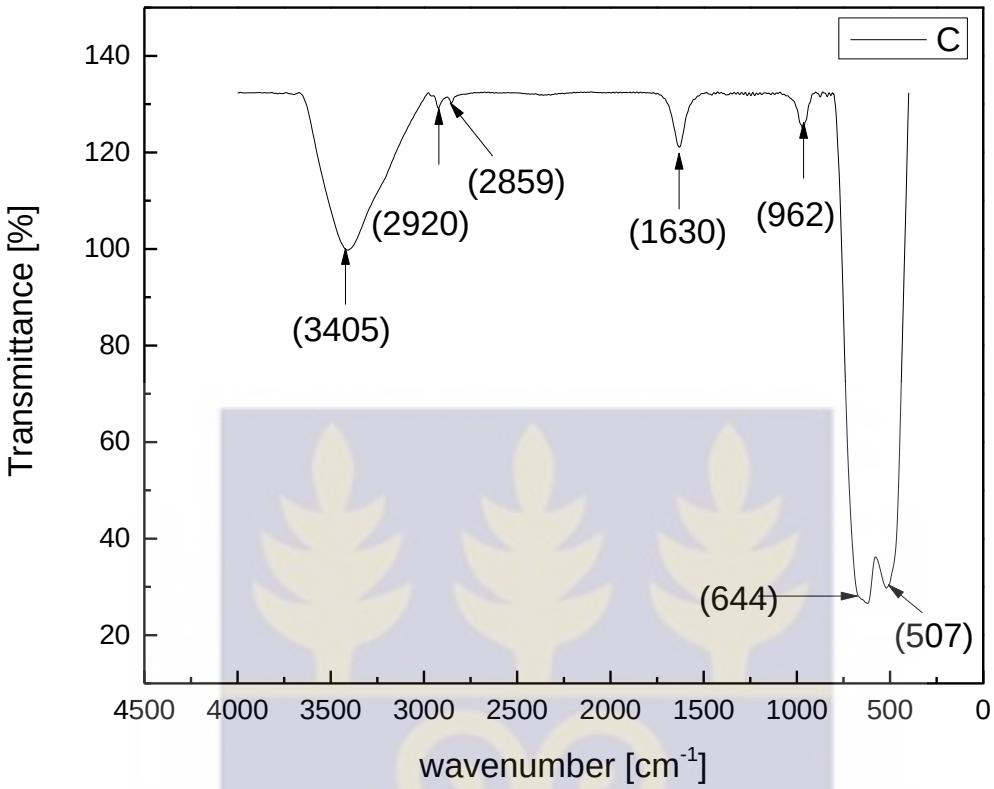

Figure 4.8: FTIR spectra of SnO_2 nanoparticles with urea as the reducing agent (C)

The peaks at 3405 cm^{-1}, 1630 cm^{-1}, and 962 cm^{-1} in the Figure 4.8 are assigned to Sn-OH bonds, H-OH bonds from the moisture content of the powder. 2920 $cm^{-1}$and 2859 cm^{-1} are attributed to alkyl CH stretching [46]. 644 cm^{-1} and 507 cm^{-1} are attributed to Sn–O stretching modes of Sn–O–Sn and Sn–OH, respectively [43, 47].

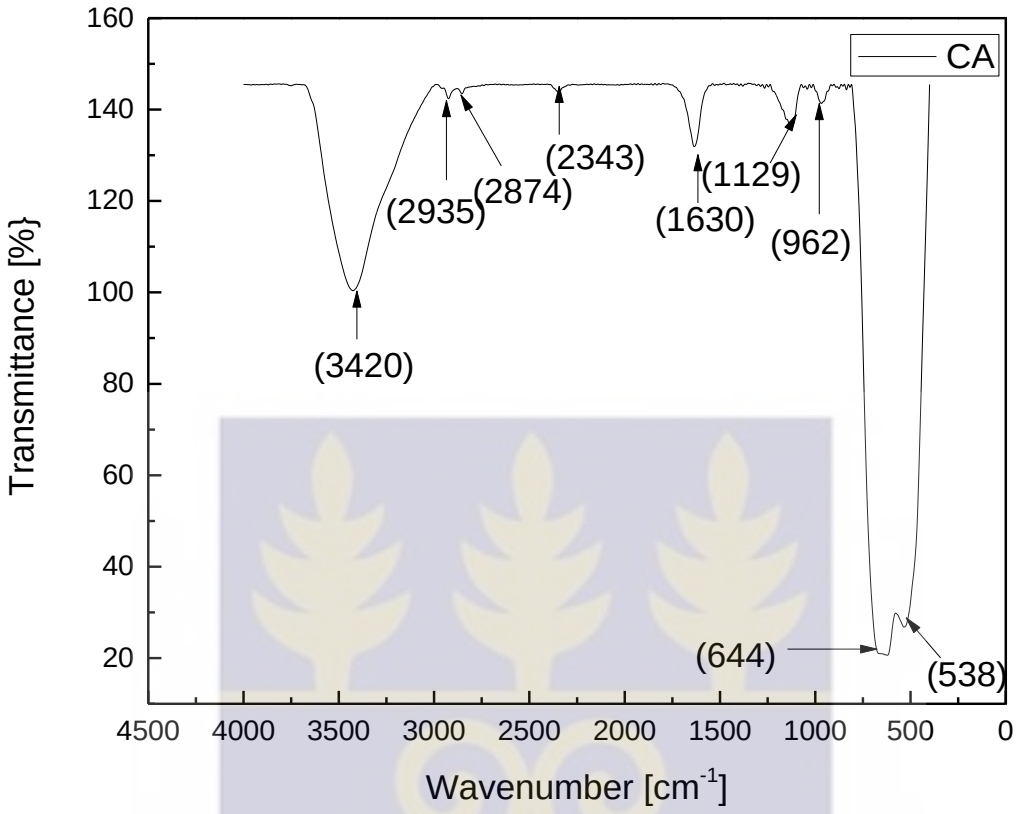

Figure 4.9: FTIR spectra of SnO_2 nanoparticles with urea as the reducing agent and AOT as the surfactant (CA)

From Figure 4.9, peaks at 644 cm^{-1} and 538 cm^{-1} are attributed to Sn–O stretching modes of Sn–O–Sn and Sn–OH, respectively. 2935 $cm^{-1}$and 2874 cm^{-1} are attributed to alkyl CH stretching. The peak at 3420 cm^{-1}, 2343 cm^{-1}, 1630 cm^{-1}, and 962 cm^{-1} are assigned to Sn-OH bonds, H-OH bonds from the moisture content of the powder [40-44].

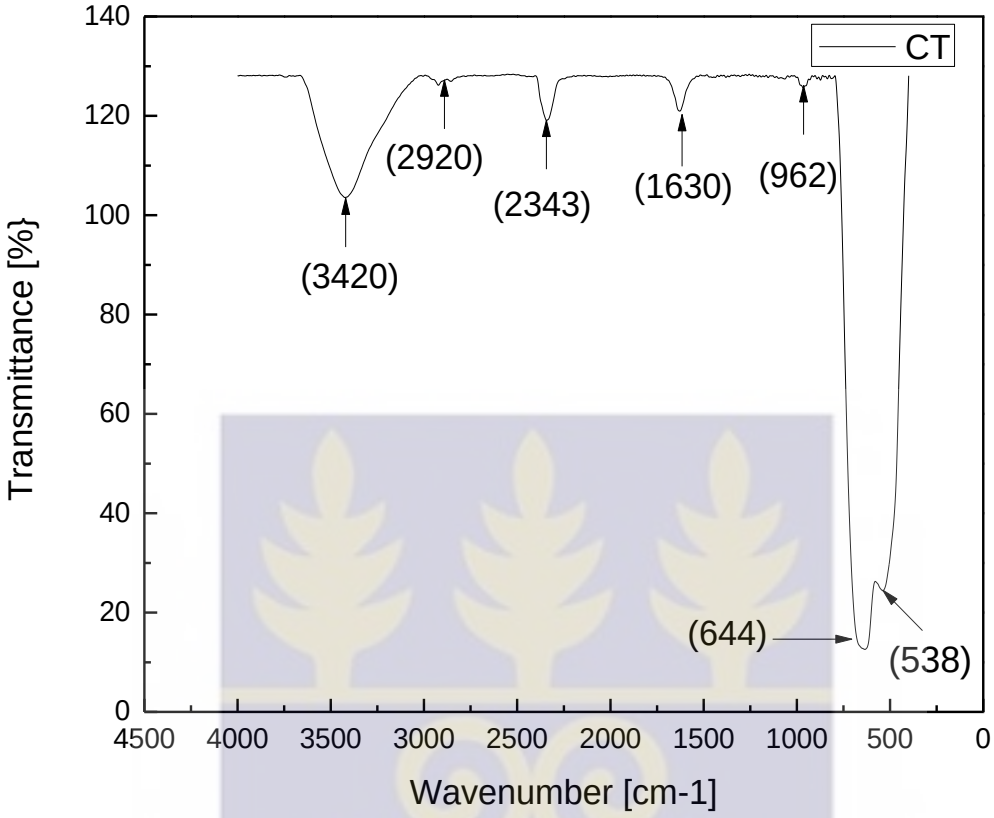

Figure 4.10: FTIR spectra of SnO_2 nanoparticles with urea as the reducing agent and AOT as the surfactant (CA)

From Figure 4.10, the peaks at 644 cm^{-1} and 538 cm^{-1} are attributed to Sn–O stretching modes of Sn–O–Sn and Sn–OH, respectively. 2935 $cm^{-1}$and 2874 cm^{-1} peaks are attributed to alkyl CH stretching. The peak at 3420 cm^{-1}, 2343 cm^{-1}, 1630 cm^{-1}, and 962 cm^{-1} are assigned to Sn-OH bonds, H-OH bonds from the moisture content of the powder [40-44].

The FTIR results in Figures 4.4 to 4.10 indicate that synthesized powder is tin oxide containing some degree of moisture, residual hydroxide and some AOT content. Residual hydroxide content is an indication of either incomplete conversion of hydrated tin oxide or some reaction between SnO_2 and H_2O due to very high surface area of the synthesized powder and the residual AOT from inadequate washing of precipitates before drying [28].

4.3 SEM micrographs of the as-synthesized SnO_2 nanoparticles

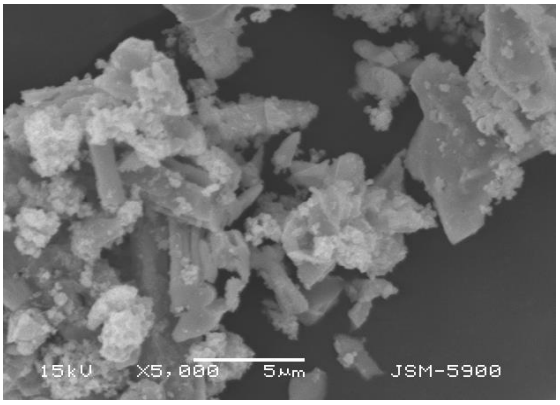

A

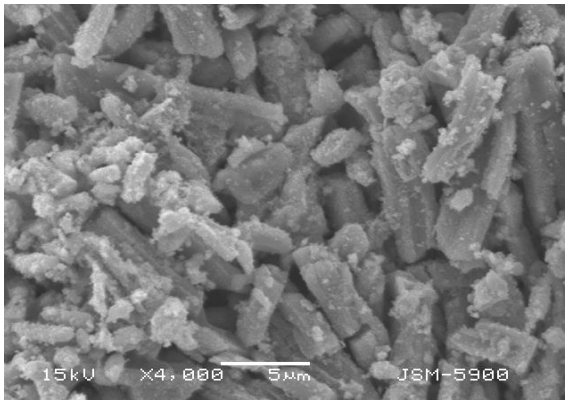

AA

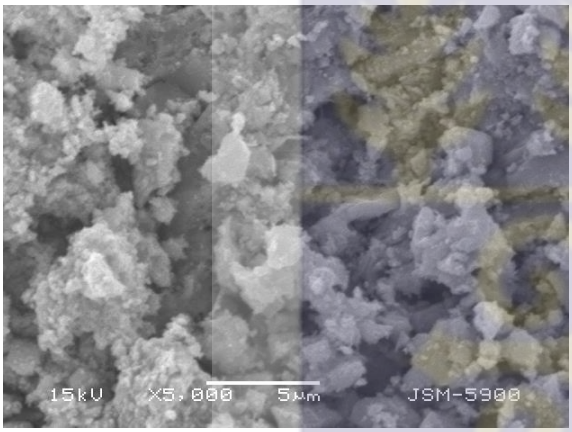

AT

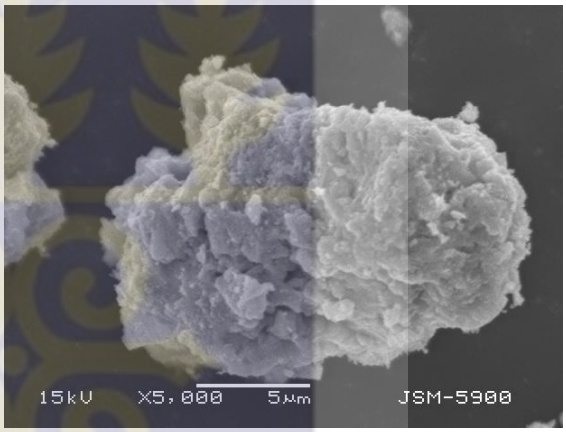

C at 5µm magnification

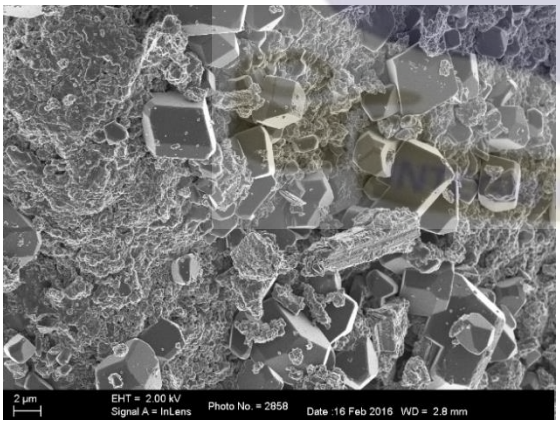

C at 1µm magnification

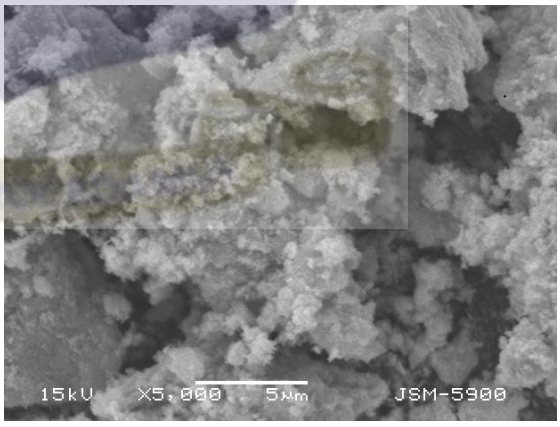

CT

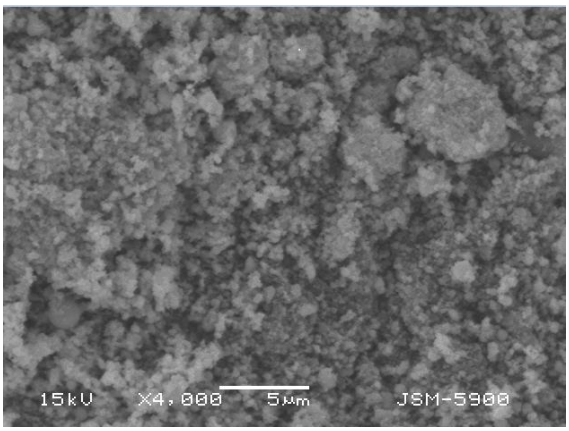

(E) at 5µm magnification

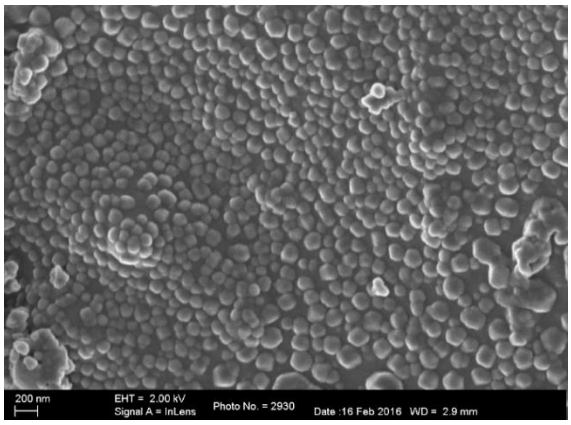

(E) at 200nm magnification

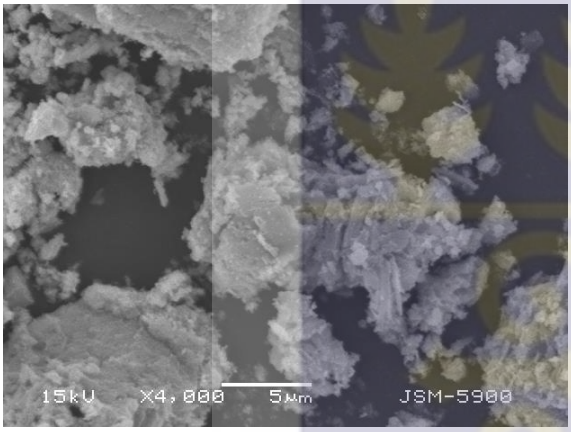

CA at 5µm magnification

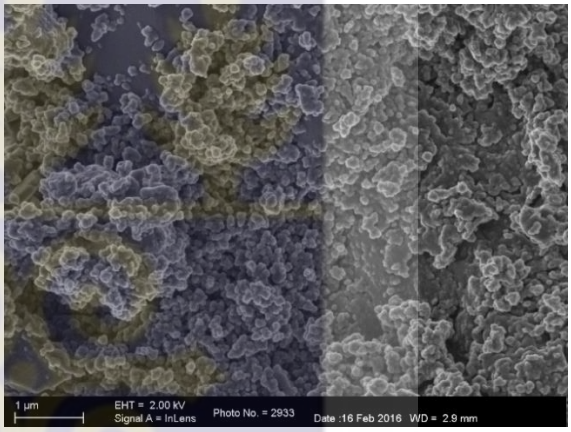

CA at 1µm magnification

Figure 4.11: SEM Micrographs of SnO_2 nanoparticles of the various treatments

The SEM micrographs in Figure 4.11 clearly shows different morphologies for SnO_2 prepared in different surfactants. The shape of the agglomerated sample C looked like florets of cauliflower. Nanorods were formed for samples A and AA. Uniform spherical-like morphologies were observed for sample E. For samples prepared with CTAB (CT and AT), agglomerated particles were formed and this is because, in an aqueous system, CTAB ionizes completely and results in cation with tetrahederal structure. The electrostatic interaction takes place between CTA^+ cations and $Sn(OH)_6^{2-}$ anions, the CTA^+ cations condense into aggregates in which counter ions are interrelated in the interfaces condense into aggregates in

which counter ions $Sn(OH)_6^{2-}$ are interrelated in the interfaces between the head group to form CTA^+- $Sn(OH)_6^{2-}$ pair[10, 47]. AOT being an anionic surfactant, it was found that there is no direct interaction between the $Sn(OH)_6^{2-}$ ions and the SO_7^- head of the AOT since both are similarly charged. Both the $Sn(OH)_6^{2-}$ nanoparticles and micelles coexist individually with no significant change in the structure of the micelles [48].

The different morphology reveals the role of individual reducing agents and surfactants in controlling the nucleation and crystal orientation.

4.4 Energy Dispersive X-ray Spectrum (EDX) Analysis of the as-synthesized SnO_2 nanoparticles.

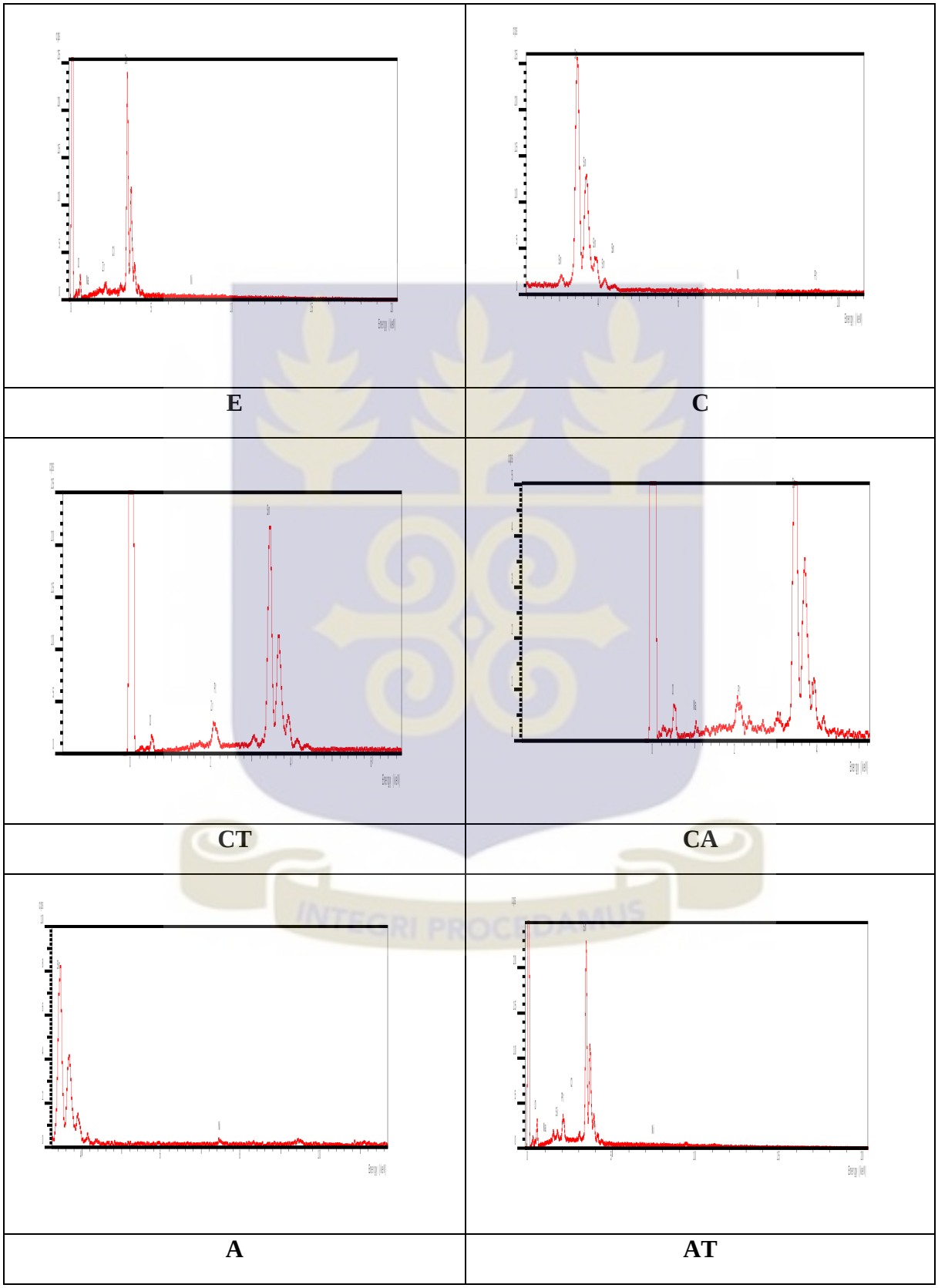

E

C

CT

CA

A

AT

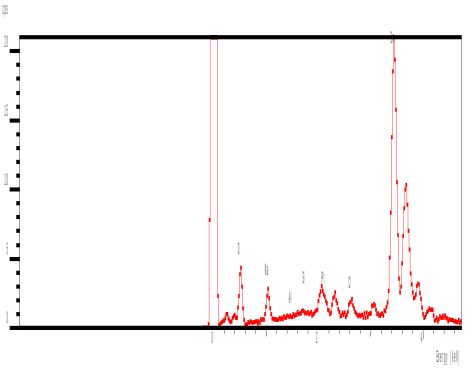

AA

Figure 4.12: EDX spectrum of SnO_2 nanoparticles of the various treatments

Table 4.2: EDX atomic % of the synthesized SnO_2 nanoparticles

Sample	Element (Atomic %)		Atomic ratio of Sn:O
	O	Sn	
A	**66.29**	**30.21**	**1:1.19**
AA	**54.95**	**30.33**	**1:1.81**
AT	**63.31**	**33.04**	**1:1.92**
C	**81.06**	**61.54**	**1:1.32**
CA	**58.37**	**36.45**	**1:1.60**
CT	**76.46**	**21.51**	**1:3.55**
E	**60.05**	**38.62**	**1:1.54**

According to the EDX analysis, the atomic ratio of Sn to O (Table 4.0) for all the treatments agrees with tin oxide being an *n*-doped semiconductor with intrinsic carrier density primarily determined by oxygen vacancies. The EDX shows that Sn and O are present which is in agreement with the XRD results [9].

4.5 Electrochemical Characterization of the obtained SnO_2 nanoparticles

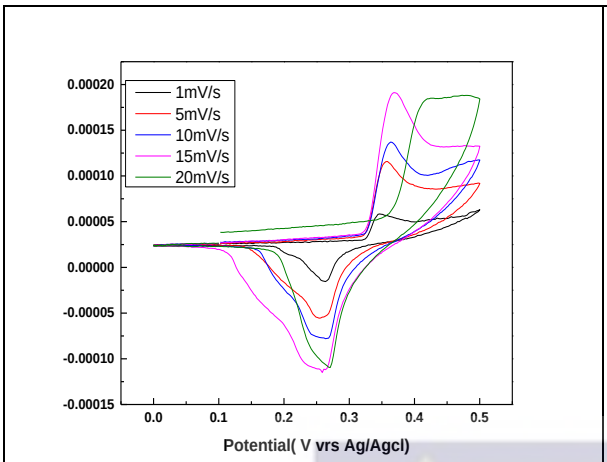

A

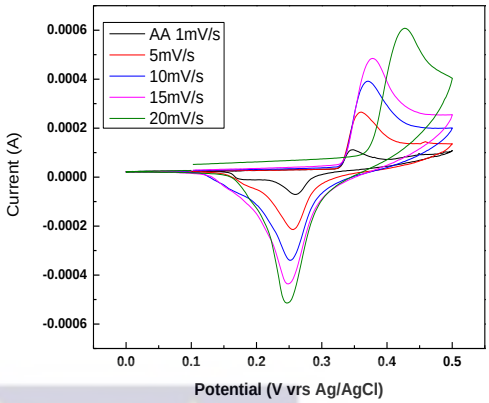

AA

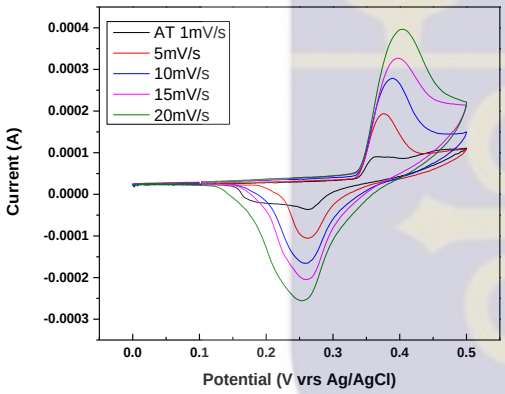

AT

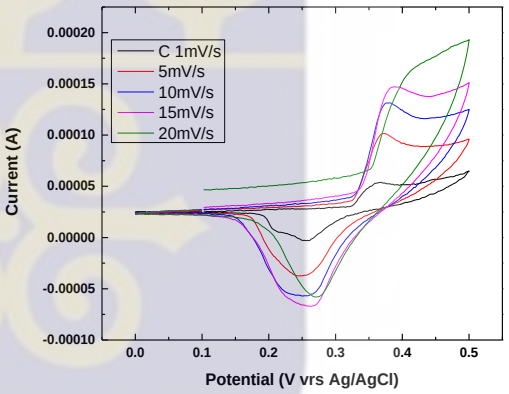

C

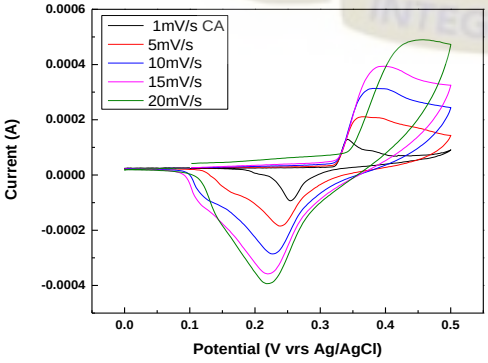

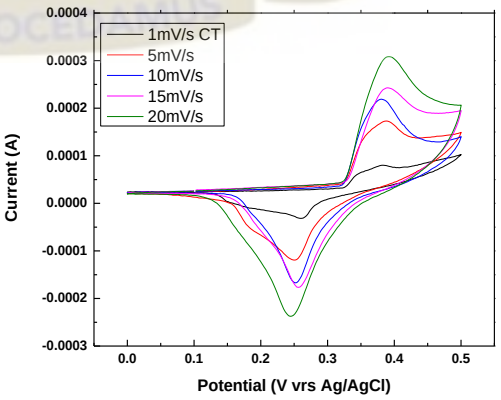

CA	CT
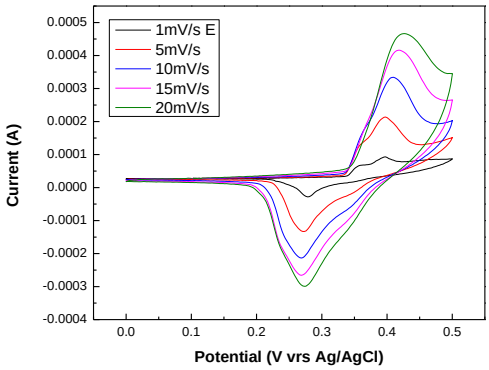	
E	

Figure 4.13: Cyclic Voltagrams of the as-obtained SnO_2 nanoparticles at different scan rates.

From the Figure 4.13 above, it can be observed that, the current under the curve increased with the increasing scan rate and this due to the reaction time being shorter and voltammetric current is increased if the reversibility is excellent [49]. Results also show two main peaks, a broad cathodic peak, and anodic peaks corresponding to redox peak of Sn^{4+}/Sn^{3+}. The electron addition process for SnO_2 semiconductor electrode can be written as [50]

$$Sn^{IV}O_2 + e^-_{(external)} + H^+_{(solution)} \rightarrow Sn^{III}O(OH^-) \quad (11)$$

Table 4.3: Capacitance values estimated from the Cyclic Voltamogram

Sample	Capacitance (F/g)		
	5 mV/s	10 mV/s	15 mV/s
A	0.5427	0.3462	0.3732
AA	1.5687	1.2358	1.036
AT	0.937	0.835	0.748

C	0.493	0.3567	0.2743
CA	1.288	1.071	0.8969
CT	0.7	0.65	0.57330
E	1.03	0.5855	0.5027

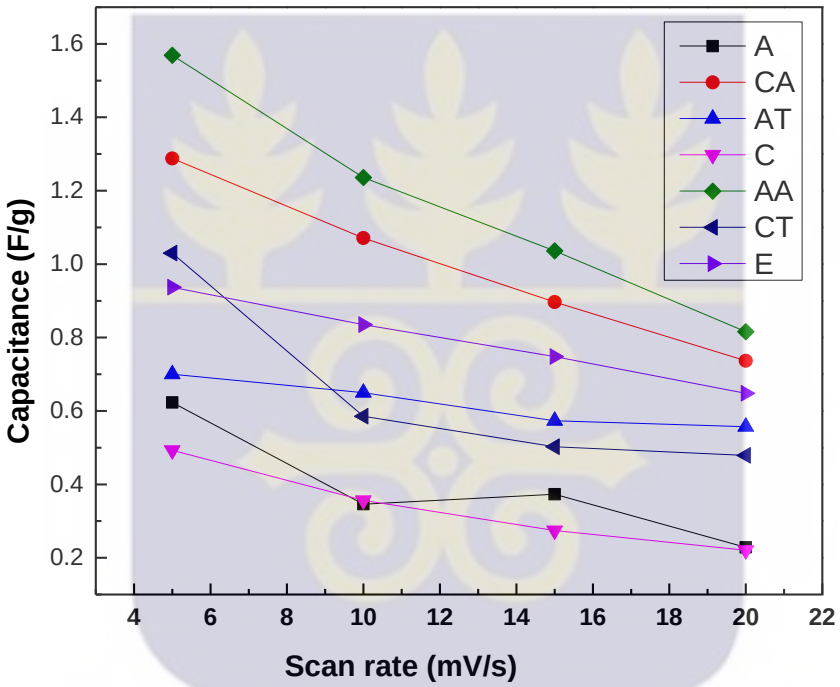

Figure 4.14: Specific capacitance of the synthesized SnO_2 particles

From Figure 4.14, the specific capacitance generally decreases with increasing scan rate. The specific decrease of capacitance with increase in scan rate can be attributed to electrolytic ions diffusing and migrating into the active materials at low scan rates. At high scan rates, the diffusion effect, limiting the migration of the electrolytic ions, causes some active surface areas to become inaccessible for charge storage [51].

Specific capacitance of the nanoparticles was calculated from cyclic voltammetry (CV) curves in Figure 4.13 using the following equation:

$$\mathbf{C_s} = \frac{i}{sm} \qquad (12)$$

where C_s is the specific capacitance, i is the average cathodic current, s is the scan rate and m is the mass of the electrode. It is reported that, the factors affecting the capacitance are particle sizes and electrochemical conditions, some of which are type of electrolyte, concentration of electrolyte and scan rate. Some other factors affecting the capacitance are surface activation under the electrochemical conditions, oxygen content on the surface, surface oxides and lattice defects resulting from the method of preparation [49]. The highest capacitance recorded for the SnO_2 nanoparticles was estimated to be 1.6 F/g at a scan rate of 5 mV/s (Table 4.3). The low values of capacitance recorded could be attributed to low conductivity of the SnO_2 nanoparticles which is evident from the high internal resistance values recorded in Table 4.4. The observed specific capacitance values are comparable with reported values of SnO_2 [33].

It can also be seen from Table 4.3 that samples with AOT (AA and CA) as the surfactant have higher capacitance than samples with CTAB (AT and CT) as the surfactant and samples without surfactant addition (A and C). This could be attributed to the fact that for samples prepared with CTAB there was agglomeration of particles, hence the porosity decreased as compared with samples prepared with AOT. This is confirmed by the SEM micrographs from Figure 4.11. Enhanced porosity allows for more electrolyte penetration and hence increases charge storage [52]. Although the average crystallite size for sample A was smaller and as such had a larger surface area compared to the other samples, it still had a lower capacitance value recorded. This could be attributed to the fact that there was less electro active surface for the transfer of electrons and diffusion of ions [53]. Since not all the specific surface area is electrochemically accessible when the material is in contact with an electrolyte, the measured capacitance of various materials does not linearly increase with increasing specific surface

area. The pore size of the electrode material plays an important role in the electrochemical active surface area. In addition, the intrinsic electrical resistance of the material may increase because the bonded heteroatom (O) possess higher reactivity, resulting in barriers to electron transfer [20].

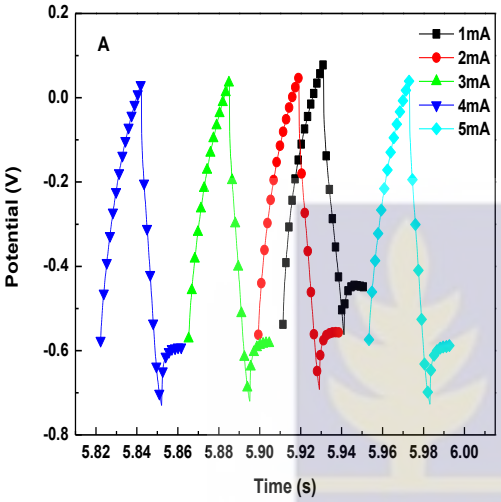

A

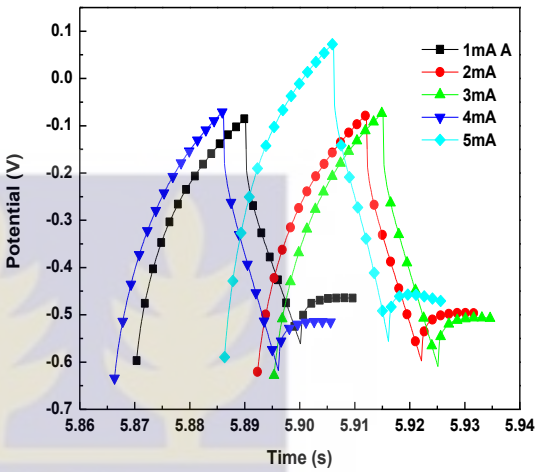

AA

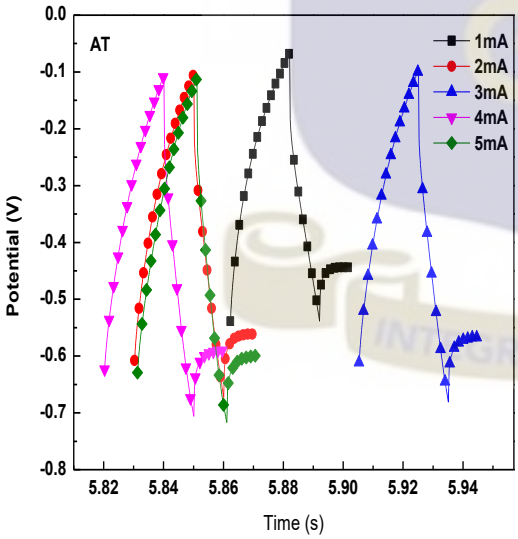

AT

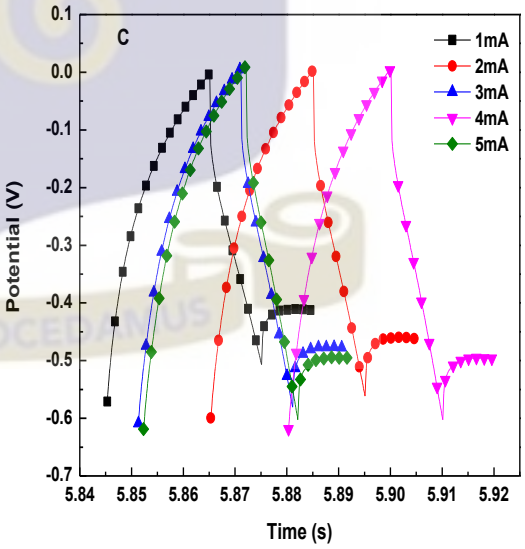

C

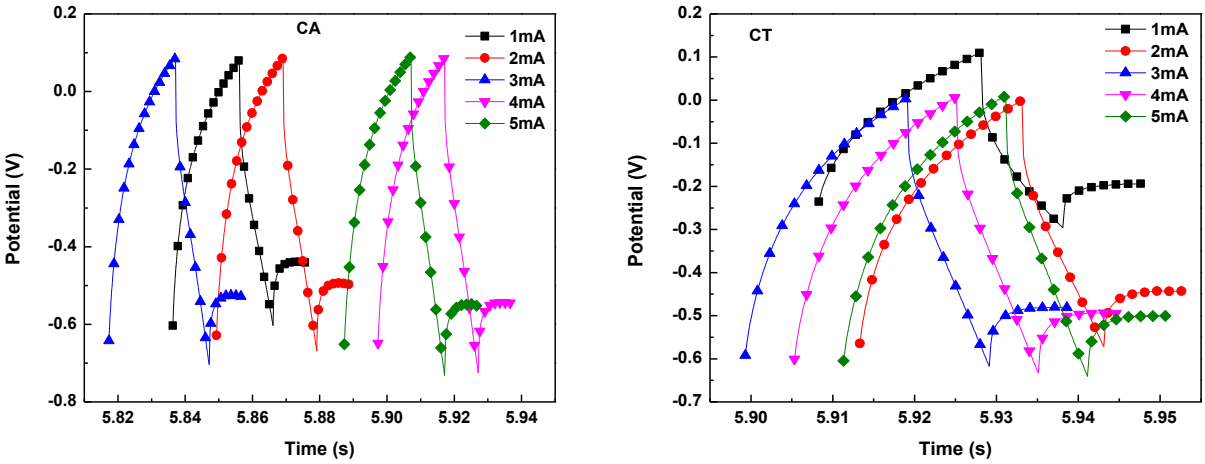

CA CT

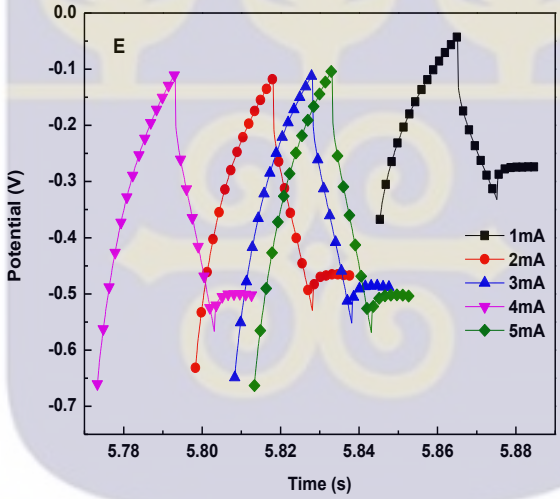

E

Figure 4.15: CCCD of the SnO_2 nanoparticles at different current densities

Table 4.4: Internal resistance values of the SnO_2 nanoparticles.

Sample	R_i (Ω)				
	1 mA	2 mA	3 mA	4 mA	5 mA
A	78.0	39.8	26.7	20.1	16.1
CA	55.0	27.8	18.5	13.8	12.8
E	59.0	30.0	20.0	15.1	12.1
AT	62.0	30.8	20.5	15.5	12.4
C	83.0	41.0	27.7	20.7	16.5
CT	62.0	32.3	21.0	16.0	12.3
AA	45.0	23.0	15.3	11.8	9.4

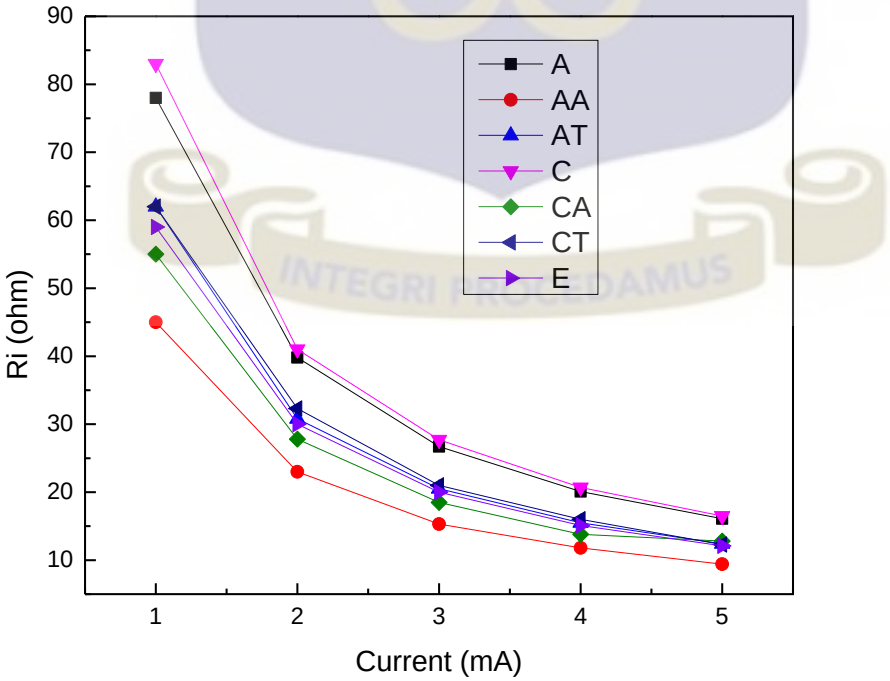

Figure 4.16: Internal resistance estimated from ohmic drop of the CCCD curves.

Table 4.5: Efficiency values of the SnO_2 nanoparticle electrodes

Sample	Columbic efficiency (η_t) %				
	1 mA	2 mA	3 mA	4 mA	5 mA
A	51.3	50.8	50.5	50.5	50.5
AA	52.3	52.3	52.3	52.3	49.7
AT	51.3	50.3	50.3	49.5	49.5
C	50.8	50.8	50.5	50.3	50.3
CA	51.8	51.0	51.3	53.9	50.3
CT	51.0	51.0	51.0	50.8	50.8

Figure 4.15 compares the charge-discharge curves of the SnO_2 particles at different currents. They all show nonlinear behavior, demonstrating the redox process of the SnO_2 particles. This is also in agreement with the cyclic voltamogram in Figure 4.13. The efficiencies η of the SnO_2 electrode material were estimated from the CCCD plots in Figure 4.15 using the equation:

$$\eta = \frac{t_D}{t_C} \qquad (13)$$

where t_D and t_C are the discharge and charge durations (s).

The low energy efficiencies are essentially related to the inability of the SnO_2 electrodes to store enough charges as result of their high internal resistance.

Table 4.6: Capacitance retention values of the SnO_2 electrode

Sample	Capacitance of 1st cycle (F/g)	Capacitance of 10th cycle (F/g)	Capacitance retention (%)
A	0.052102083	0.016265957	31.21939931
AA	0.04552381	0.018005556	39.55195258
AT	0.04866875	0.015778723	32.42064652
C	0.066546939	0.018553191	27.87985718
CA	0.066688421	0.024827083	37.22847676
CT	0.049791579	0.015761538	31.65502841
E	0.037070526	0.012644048	34.10808768

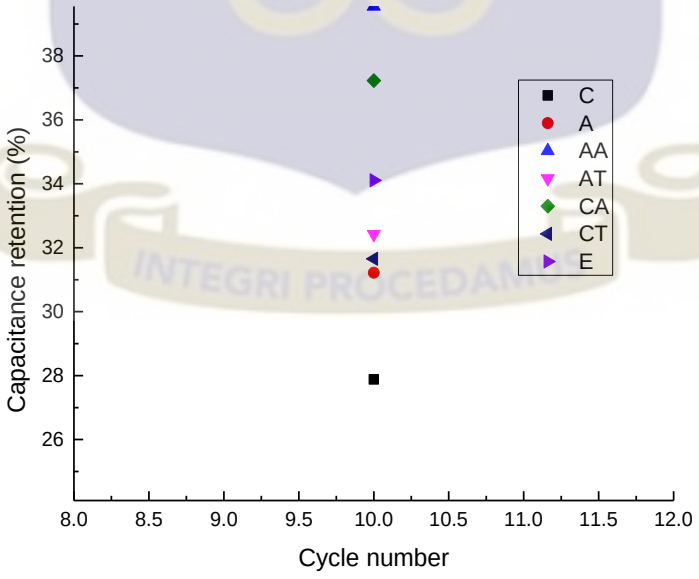

Figure 4.17: Capacitance retention of the SnO_2 electrodes after 10cycles

The capacitance retention (Figure 4.17) was estimated from the CCCD curves in Figure 4.15 by using the equation

$$\text{Capacitance retention} = \frac{\text{capacitance of the first cycle}}{\text{capacitance of the 10th cycle}} X 100\% \quad (14)$$

The capacitance retention also agrees with the discussions made for Figures 4.14.

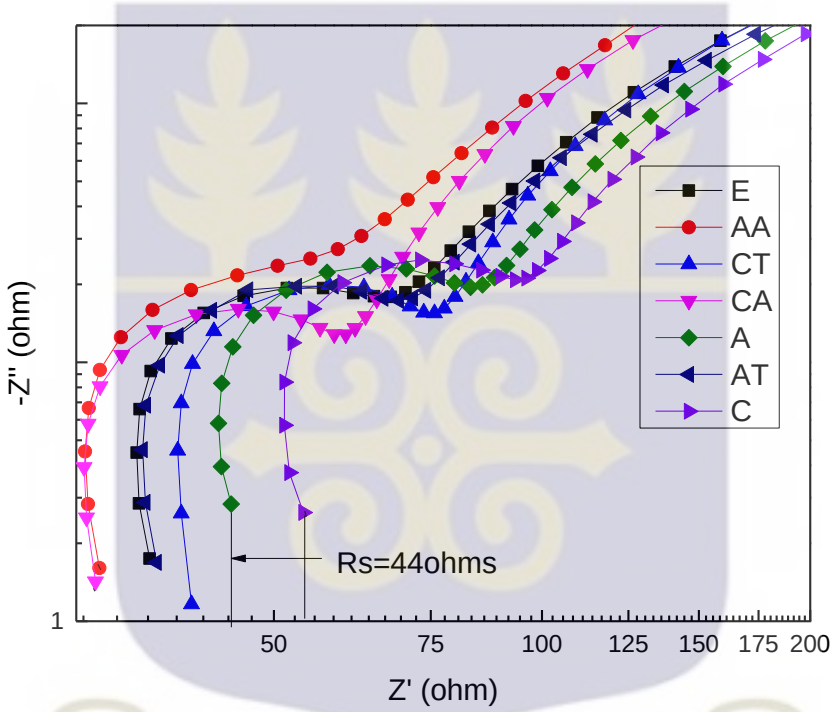

Figure 4.18: The Nyquist plot for the as-synthesized SnO_2 nanoparticles

Figure 4.18 shows the Nyquist plot, which represents the real and imaginary parts of the impedance in a sample. The x-axis intercept in the high frequency region corresponds to the resistance of the electrolyte solution (R_s) which is also referred to as the equivalent series resistance (ESR), which consist of the resistance of the aqueous electrolyte, the intrinsic resistance of the SnO_2 electrode, and the contact resistance at the electrode. The impedance spectra usually show a single semicircle in the high frequency region and nearly vertical line in the low frequency region for a supercapacitor, which indicates that the electrode process is

controlled by electrochemical reaction at high frequencies and by mass transfer at low frequencies [43]. The origin of the semi-circle at higher frequency range is due to ionic charge transfer resistance (R_{ct}) at the electrode–electrolyte interface. The diameter of the semi-circle along the real axis (Z_{dia}) gives the R_{ct} [54]. It is also worth mentioning that for ideal supercapacitors, the Nyquist plot should be a line perpendicular to the real axis at low frequency. It also confirms the fact that porosity affects the electrolyte interaction with the SnO_2 particles which in turn affects the capacitance. The ESR for the samples increase accordingly as CA (31.5 Ω) <AA (31.85 Ω) <E (36.3 Ω) <AT (36.92 Ω) <CT (40.41 Ω) <C (53.97 Ω). These values are confirmation for the low capacitance, efficiencies and capacitance retention recorded in Tables 4.3, 4.5 and 4.6. The reasons for this observation are the same as explained for the capacitance.

CHAPTER FIVE

5.0 Conclusions and Recommendations

5.1 Conclusions

SnO_2 nanoparticles were successfully synthesized with both the Water-in-Oil microemulsion and the hydrothermal techniques with both techniques giving crystalline particles with average crystallite size in the range of 2 nm to 10 nm. Samples with surfactants addition exhibited higher capacitances than samples without surfactant addition, however samples with surfactant AOT exhibited better capacitance than samples with surfactant CTAB due to less agglomeration. From the capacitance results we can say that the addition of surfactant AOT helps to improve the capacitance performance of SnO_2 nanoparticles. The general low capacitance recorded for the SnO_2 nanoparticles from the various treatments can be attributed to the low conductivity of SnO_2.

From the results obtained we can also conclude that Sodium borohydride acts as a good reducing agent in producing SnO_2 particles with good crystallinity, high surface area and good pore structure for supercapacitor electrode material than Urea. Also, SnO_2 particles prepared by the hydrothermal route using Sodium borohydride as the reducing agent exhibit better supercapacitor properties than particles prepared by the water-in-Oil microemulsions route. The type of surfactant and reducing agent used also influenced the particle size and the morphology which in turn influenced the capacitance of the SnO_2 nanoparticles. To finally conclude, we can say that a higher surface area does not always mean a higher capacitance.

5.2 Recommendation

There is still the need for developing alternative efficient electrode binders capable of improving the SnO_2 electrode performance. Activated carbon materials with high BET

surface area and excellent electrical conductivity can be added to the SnO_2 naoparticles to improve the conductivity of the SnO_2 nanoparticles.

REFERENCES

1. Cheng, Q., Tang, J., Ma, J., Zhang, H., Shinya, N. and Qin, L.C. (2011). Graphene and nanostructured MnO_2 composite electrodes for supercapacitors. *Carbon, 49*(9), 2917-2925.

2. Hwang, S.W. and Hyun, S.H. (2007). Synthesis and characterization of tin oxide/carbon aerogel composite electrodes for electrochemical supercapacitors. *Journal of Power Sources, 172*(1), 451-459.

3. Zhang, Y. X., Huang, M., Li, F. and Wen, Z. Q. (2013). Controlled synthesis of hierarchical CuO nanostructures for electrochemical capacitor electrodes. *Int. J. Electrochem. Sci, 8*, 8645-8661.

4. Bello, A., Fashedemi, O. O., Lekitima, J. N., Fabiane, M., Dodoo-Arhin, D., Ozoemena, K. I. and Manyala, N. (2013). High-performance symmetric electrochemical capacitor based on graphene foam and nanostructured manganese oxide. *AIP Advances, 3*(8), 082118.

5. Bello, A., Manyala, N., Barzegar, F., Khaleed, A. A., Momodu, D. Y. and Dangbegnon, J. K. (2016). Renewable pine cone biomass derived carbon materials for supercapacitor application. *RSC Advances, 6*(3), 1800-1809.

6. Hu, C.C., Chang, K.H. and Wang, C.C. (2007). Two-step hydrothermal synthesis of Ru–Sn oxide composites for electrochemical supercapacitors. *Electrochimica acta, 52*(13), 4411-4418.

7. Jayalakshmi, M. and Balasubramanian, K. (2008). Simple capacitors to supercapacitors-an overview. *Int. J. Electrochem. Sci, 3*(11), 1196-1217.

8. Chen, D. and Gao, L. (2004). Facile synthesis of single-crystal tin oxide nanorods with tunable dimensions via hydrothermal process. *Chemical physics letters, 398*(1), 201-206.

9. Chen, D. and Gao, L. (2004). Novel synthesis of well-dispersed crystalline SnO_2 nanoparticles by water-in-oil microemulsion-assisted hydrothermal process. *Journal of colloid and interface science, 279*(1), 137-142.

10. Gnanam, S. and Rajendran, V. (2010). Anionic, cationic and nonionic surfactants-assisted hydrothermal synthesis of tin oxide nanoparticles and their photoluminescence property. *Digest Journal of Nanomaterials and Biostructures, 5*(2), 623.

11. Patil, S. D. (2006). *Fundamental aspects of regenerative cerium oxide nanoparticles and their applications in nanobiotechnology*. University of Central Florida Orlando, Florida.

12. Díaz Delgado, R. (2002). *Tin oxide gas sensors: an electrochemical approach*: Universitat de Barcelona.

13. Roduner, E. (2006). Size matters: why nanomaterials are different. *Chemical Society Reviews, 35*(7), 583-592.

14. Mendes, P. G., Moreira, M. L., Tebcherani, S. M., Orlandi, M. O., Andrés, J., Li, M. S., Longo, E. (2012). SnO_2 nanocrystals synthesized by microwave-assisted hydrothermal method: towards a relationship between structural and optical properties. *Journal of Nanoparticle Research, 14*(3), 1-13.

15. Kong, L., Ma, J., Zhu, Z., Luan, C., Yu, X. and Yu, Q. (2010). Synthesis of orthorhombic structure epitaxial tin oxide film. *Materials letters, 64*(12), 1350-1353.

16. Batzill, M. and Diebold, U. (2005). The surface and materials science of tin oxide. *Progress in surface science, 79*(2), 47-154.

17. Winter, M. and Brodd, R. J. (2004). What are batteries, fuel cells, and supercapacitors? *Chemical reviews, 104*(10), 4245-4270.

18. Zhang, L. L. and Zhao, X. (2009). Carbon-based materials as supercapacitor electrodes. *Chemical Society Reviews, 38*(9), 2520-2531.

19. Wang, C.C. and Hu, C.C. (2005). Electrochemical and textural characterization of binary Ru–Sn oxides synthesized under mild hydrothermal conditions for supercapacitors. *Electrochimica acta, 50*(13), 2573-2581.

20. Wang, G., Zhang, L. and Zhang, J. (2012). A review of electrode materials for electrochemical supercapacitors. *Chemical Society Reviews, 41*(2), 797-828.

21. Ohno, H. and Fukumoto, K. (2008). Progress in ionic liquids for electrochemical reaction matrices. *Electrochemistry, 76*(1), 16-23.

22. Galiński, M., Lewandowski, A. and Stępniak, I. (2006). Ionic liquids as electrolytes. *Electrochimica acta, 51*(26), 5567-5580.

23. Conway, B. E. (1991). Transition from "supercapacitor" to "battery" behavior in electrochemical energy storage. *Journal of the Electrochemical Society, 138*(6), 1539-1548.

24. Zhang, S. and Pan, N. (2015). Supercapacitors performance evaluation. *Advanced Energy Materials, 5*(6).

25. Gude, K. (2013). Synthesis characterization and applications of colloidal supported metal nanoparticles.

26. Jin, X., He, B., Miao, J., Zhang, Q. and Niu, L. (2012). Stabilization and dispersion of PtRu and Pt nanoparticles on multiwalled carbon nanotubes using phosphomolybdic acid, and the use of the resulting materials in a direct methanol fuel cell. *Carbon, 50*(8), 3083-3091.

27. Domine, M. E., Hernández-Soto, M. C., Navarro, M. T. and Pérez, Y. (2011). Pt and Pd nanoparticles supported on structured materials as catalysts for the selective reductive amination of carbonyl compounds. *Catalysis today, 172*(1), 13-20.

28. Beller, M., Fischer, H., Kühlein, K., Reisinger, C.P. and Herrmann, W. (1996). First palladium-catalyzed Heck reactions with efficient colloidal catalyst systems. *Journal of organometallic chemistry*, *520*(1), 257-259.

29. Proch, S., Herrmannsdörfer, J., Kempe, R., Kern, C., Jess, A., Seyfarth, L. and Senker, J. (2008). Pt@ MOF-177: Synthesis, Room-Temperature Hydrogen Storage and Oxidation Catalysis. *Chemistry–A European Journal*, *14*(27), 8204-8212.

30. Byrappa, K. and Adschiri, T. (2007). Hydrothermal technology for nanotechnology. *Progress in Crystal Growth and Characterization of Materials*, *53*(2), 117-166.

31. Jain, K., Shrivastava, A. and Rashmi, R. (2006). Synthesis and Controlling the Morphology of SnO_2 Nanocrystals via Hydrothermal Treatment. *ECS Transactions*, *1*(21), 1-7.

32. Zielińska-Jurek, A., Reszczyńska, J., Grabowska, E. and Zaleska, A. (2012). Nanoparticles preparation using microemulsion systems. *Microemulsions—An Introduction to Properties and Applications (InTech, Poland, 2012)*, 235.

33. Boutonnet, M., Kizling, J., Stenius, P. and Maire, G. (1982). The preparation of monodisperse colloidal metal particles from microemulsions. *Colloids and Surfaces*, *5*(3), 209-225.

34. Tadros, T. F. (2009). Emulsion science and technology: a general introduction. *Emulsion science and technology*, 1-56.

35. Wang, H.Y., Liu, G.Y., Yang, Z.Z., Wang, B.-Y., Chen, L. and Jiang, Q.C. (2013). Facile Synthesis of Mesoporous SnO_2 Submicrospheres by Microemulsion Approach as High-Capacity Anodes Material for Lithium-Ion Batteries. *Int. J. Electrochem. Sci*, *8*, 2345-2353.

36. Song, K. C. and Kim, J. H. (1999). Preparation of nanosize tin oxide particles from water-in-oil microemulsions. *Journal of colloid and interface science, 212*(1), 193-196.

37. Blak, D., Windover, D., Henins, A., Gil, A. and Cline, J. (2010). Standard Reference Material 640d for X-Ray Metrology. *National Institute of Standards and Technology, Gaithersburg, MD*.

38. Caglioti, G., Paoletti, A. t. and Ricci, F. (1958). Choice of collimators for a crystal spectrometer for neutron diffraction. *Nuclear Instruments, 3*(4), 223-228.

39. Scardi, P. and Leoni, M. (2002). Whole powder pattern modelling. *Acta Crystallographica Section A: Foundations of Crystallography, 58*(2), 190-200.

40. Leoni, M., Confente, T. and Scardi, P. (2006). PM2K: a flexible program implementing Whole Powder Pattern Modelling. *Z. Kristallogr. Suppl, 23*, 249-254.

41. Jiang, L., Sun, G., Zhou, Z., Sun, S., Wang, Q., Yan, S. and Zhou, B. (2005). Size-controllable synthesis of monodispersed SnO_2 nanoparticles and application in electrocatalysts. *The Journal of Physical Chemistry B, 109*(18), 8774-8778.

42. Zhang, J. and Gao, L. (2004). Synthesis and characterization of nanocrystalline tin oxide by sol–gel method. *Journal of solid state chemistry, 177*(4), 1425-1430.

43. Song, K. C. and Kang, Y. (2000). Preparation of high surface area tin oxide powders by a homogeneous precipitation method. *Materials letters, 42*(5), 283-289.

44. Özer, M. O., Suvaci, E. and Doğan, A. (2011). Formation Mechanism of Nanosized Tin Oxide (SnO_2) Powder During Hydrothermal Synthesis. *Anadolu University Journal of Science and Technology–A Applied Sciences and Engineering, 12*(1), 25-36.

45. Sun, Y.F., Liu, S.B., Meng, F.L., Liu, J.Y., Jin, Z., Kong, L.T. and Liu, J.H. (2012). Metal oxide nanostructures and their gas sensing properties: a review. *Sensors, 12*(3), 2610-2631.

46. Tan, L., Wang, L. and Wang, Y. (2011). Hydrothermal synthesis of SnO_2 nanostructures with different morphologies and their optical properties. *Journal of Nanomaterials, 2011*, 23.

47. Blessi, S., Sonia, M. M. L., Vijayalakshmi, S. and Pauline, S. Preparation and characterization of SnO_2 nanoparticles by hydrothermal method.

48. Kumar, S. and Aswal, V. (2010). Tuning of nanoparticle–surfactant interactions in aqueous system. *Journal of Physics: Condensed Matter, 23*(3), 035101.

49. Channu, V. S. R., Holze, R., Wicker Sr, S. A., Walker Jr, E. H., Williams, Q. L. and Kalluru, R. R. (2011). Synthesis and characterization of (Ru-Sn)O_2 nanoparticles for supercapacitors. *Materials Sciences and Applications, 2*(09), 1175.

50. Venugopal, N., Saiprakash, P., Jayalakshmi, M., Ram Reddy, Y. and Rao, M. M. (2013). A study on the effect of nanosized tin oxide on the electrochemical performance of nanosized nickel hydroxide in alkali solution. *Journal of Experimental Nanoscience, 8*(5), 684-693.

51. Li, H., Yu, M., Wang, F., Liu, P., Liang, Y., Xiao, J. and Yang, G. (2013). Amorphous nickel hydroxide nanospheres with ultrahigh capacitance and energy density as electrochemical pseudocapacitor materials. *Nature communications, 4*, 1894.

52. Leoni, M., Confente, T. and Scardi, P. (2006). PM2K: a flexible program implementing Whole Powder Pattern Modelling. *Z. Kristallogr. Suppl, 23*, 249-254.

53. Sun, Y.F., Liu, S.B., Meng, F.L., Liu, J.-Y., Jin, Z., Kong, L.T. and Liu, J.H. (2012). Metal oxide nanostructures and their gas sensing properties: a review. *Sensors, 12*(3), 2610-2631.

54. Yang, D. (2012). *Application of nanocomposites for supercapacitors: characteristics and properties*: INTECH Open Access Publisher.